Icarus 234 (2014) 17–35

Contents lists available at ScienceDirect

Icarus

journal homepage: www.elsevier.com/locate/icarus

Thermal infrared observations and thermophysical characterization of OSIRIS-REx target asteroid (101955) Bennu

J.P. Emery [a,*], Y.R. Fernández [b], M.S.P. Kelley [c], K.T. Warden (nèe Crane) [a,1], C. Hergenrother [d], D.S. Lauretta [d], M.J. Drake [d], H. Campins [b], J. Ziffer [e]

[a] Earth and Planetary Science Department, Planetary Geosciences Institute, University of Tennessee, Knoxville, TN 37996, United States
[b] Physics Department, University of Central Florida, Orlando, FL 32816, United States
[c] Department of Astronomy, University of Maryland, College Park, MD 20742-2421, United States
[d] Department of Planetary Sciences, University of Arizona, Tucson, AZ 85721, United States
[e] Department of Physics, University of Southern Maine, Portland, ME 04104, United States

ARTICLE INFO

Article history:
Received 29 November 2013
Revised 5 February 2014
Accepted 7 February 2014
Available online 21 February 2014

Keywords:
Asteroids, surfaces
Regoliths
Infrared observations
Near-Earth objects
Spectrophotometry

ABSTRACT

Near-Earth Asteroids (NEAs) have garnered ever increasing attention over the past few years due to the insights they offer into Solar System formation and evolution, the potential hazard they pose, and their accessibility for both robotic and human spaceflight missions. Among the NEAs, carbonaceous asteroids hold particular interest because they may contain clues to how the Earth got its supplies of water and organic materials, and because none has yet been studied in detail by spacecraft. (101955) Bennu is special among NEAs in that it will not only be visited by a spacecraft, but the OSIRIS-REx mission will also return a sample of Bennu's regolith to Earth for detailed laboratory study. This paper presents analysis of thermal infrared photometry and spectroscopy that test the hypotheses that Bennu is carbonaceous and that its surface is covered in fine-grained (sub-cm) regolith. The Spitzer Space Telescope observed Bennu in 2007, using the Infrared Spectrograph (IRS) to obtain spectra over the wavelength range 5.2–38 μm and images at 16 and 22 μm at 10 different longitudes, as well as the Infrared Array Camera (IRAC) to image Bennu at 3.6, 4.5, 5.8, and 8.0 μm, also at 10 different longitudes. Thermophysical analysis, assuming a spherical body with the known rotation period and spin-pole orientation, returns an effective diameter of 484 ± 10 m, in agreement with the effective diameter calculated from the radar shape model at the orientation of the Spitzer observations (492 ± 20 m, Nolan, M.C., Magri, C., Howell, E.S., Benner, L.A.M., Giorgini, J.D., Hergenrother, C.W., Hudson, R.S., Lauretta, D.S., Margo, J.-L., Ostro, S.J., Scheeres, D.J. [2013]. Icarus 226, 629–640) and a visible geometric albedo of 0.046 ± 0.005 (using H_v = 20.51, Hergenrother, C.W. et al. [2013]. Icarus 226, 663–670). Including the radar shape model in the thermal analysis, and taking surface roughness into account, yields a disk-averaged thermal inertia of 310 ± 70 J m^{-2} K^{-1} s$^{-1/2}$, which is significantly lower than several other NEAs of comparable size. There may be a small variation of thermal inertia with rotational phase (±60 J m^{-2} K^{-1} s$^{-1/2}$). The spectral analysis is inconclusive in terms of surface mineralogy; the emissivity spectra have a relatively low signal-to-noise ratio and no spectral features are detected. The thermal inertia indicates average regolith grain size on the scale of several millimeters to about a centimeter. This moderate grain size is also consistent with low spectral contrast in the 7.5–20 μm spectral range. If real, the rotational variation in thermal inertia would be consistent with a change in average grain size of only about a millimeter. The thermophysical properties of Bennu's surface appear to be fairly homogeneous longitudinally. A search for a dust coma failed to detect any extended emission, putting an upper limit of about 10^6 g of dust within 4750 km of Bennu. Three common methodologies for thermal modeling are compared, and some issues to be aware of when interpreting the results of such models are discussed. We predict that the OSIRIS-REx spacecraft will find a low albedo surface with abundant sub-cm sized grains, fairly evenly distributed in longitude.

* Corresponding author. Fax: +1 865 974 2368.
E-mail address: jemery2@utk.edu (J.P. Emery).
[1] Current address: Department of Earth, Atmospheric, and Planetary Science, Purdue University, West Lafayette, IN 47907, United States.

http://dx.doi.org/10.1016/j.icarus.2014.02.005
0019-1035/

1. Introduction

As our closest cosmic neighbors, Near-Earth Asteroids (NEAs) have been the focus of much attention ever since the discovery of (433) Eros just before the turn of the 20th century. Recent years have seen a steady rise in the level of interest in NEAs, due mainly to the combination of increasing observational sensitivity for detection and characterization along with growing recognition of their relevance for understanding dynamical and collisional processes and of the potential hazard they pose to Earth. The population of known NEAs currently stands at more than 10,000 (Minor Planet Center[2]). This large number enables broad statistical studies of physical properties and separation of sub-populations. Albedos and visible spectra indicate that ~22% of NEAs belong to the S taxonomic complex that dominates the inner part of the Main Belt of asteroids, and ~10% belong to the C-complex that dominates the middle and outer Main Belt (Stuart and Binzel, 2004; DeMeo and Carry, 2013). Whereas most NEAs appear to have been nudged out of the Main Belt by the ν_6 and 3:1 resonances, a significant fraction could have come from the outer Main Belt or even Jupiter family comet orbits (Bottke et al., 2002). There is also mounting evidence that smaller (<few km) NEAs have fresher surfaces, as measured by spectral class (Binzel et al., 2004a, 2010) and albedo (Trilling et al., 2010; Mainzer et al., 2011a). Anchoring statistical studies with more detailed physical characterization of representative objects adds critical extra dimensions for understanding the population. The proximity of NEAs enables ready access for detailed analysis in the form of spacecraft missions, as evidenced by the highly successful missions by NASA and JAXA to the S-type NEAs (433) Eros and (25143) Itokawa. Low-albedo, potentially primitive, NEAs are high priority for similarly detailed characterization.

One of the most intriguing NEAs for detailed physical characterization is (101955) Bennu (1999 RQ_{36}). Bennu is categorized as a potentially hazardous asteroid (PHA), with a relatively high probability of impact with Earth in the late 22nd century (cumulative impact probability of 3.7×10^{-4}, Chesley et al., in press; Milani et al., 2009). Spectrally, Bennu is a B-class object characterized by a linear, featureless spectrum from 0.5 to 2.5 μm with a neutral to bluish spectral slope (Clark et al., 2011; Davies et al., 2007; Bus and Binzel, 2002). Among the asteroid population, B-class objects most commonly reside in the middle to outer Main Belt (DeMeo and Carry, 2013), but the inner main Belt also contains a substantial population. They are thought to be primitive, volatile-rich remnants from the early Solar System, similar to the CI and CM carbonaceous chondrites. The B-class includes many intriguing objects such as (2) Pallas, the second largest asteroid, (24) Themis, the largest member of the Themis family, and (3200) Phaethon, the parent of the Gemenid meteor shower (e.g., de León et al., 2010). Spectroscopy of B-class objects suggests surface constituents are anhydrous silicates, hydrated silicates (phyllosilicates), organic polymers, magnetite, and sulfides (Larson et al., 1983; Clark et al., 2010; Ziffer et al., 2011; de León et al., 2012), and those in the outer Main Belt may support H_2O ice (Rivkin and Emery, 2010; Campins et al., 2010a). Dynamically and spectrally, Bennu itself is likely related to a population of B-type asteroids in the inner belt (e.g., Campins et al., 2010b; Walsh et al., 2013). The spectrum of Bennu exhibits an upturn longward of 2 μm, interpreted as a thermal tail and suggesting a low albedo (Clark et al., 2011). Radar observations from Goldstone and Arecibo in 1999 and 2005 resolved the shape and size, indicating a roughly spheroidal, "spinning top" shape, a mean diameter of 492 ± 20 m, and an obliquity of ~180° (Nolan et al., 2013). Lightcurve observations reveal a rotation period of 4.29746 ± 0.002 h and a small amplitude also indicating a nearly spherical shape (Hergenrother et al., 2013; Nolan et al., 2013).

In addition to its appeal as a potentially primitive asteroid and PHA, Bennu is one of the more readily accessible spacecraft targets. It has a low inclination (~6°), low eccentricity (~0.2) orbit that brings it close to Earth every six years ($a \sim 1.13$ AU). This arrangement results in a series of possible low-energy transfer orbits for rendezvous and Earth return (e.g., Binzel et al., 2004b) and ensures a well-constrained thermal environment for spacecraft operations. The spheroidal shape measured by radar suggests a relatively uniform gravity field. The rotation period is slow enough for the asteroid to support regolith and to allow sampling operations. Based largely on these considerations, Bennu was chosen as the target for the OSIRIS-REx sample return mission, the third mission in the NASA New Frontiers program. Samples from the regolith of Bennu will be returned to Earth in order to understand the origin and nature of volatile and organic material in the early Solar System.

Thermal emission data of asteroids contain a wealth of information about the physical properties of the bodies and their surface. Radiometry is widely used to determine the sizes and albedos of asteroids from photometric measurements of thermal and visible flux (e.g., Morrison, 1973, 1974; Lebofsky and Spencer, 1989; Tedesco et al., 2002; Mainzer et al., 2011b). This technique is most accurate when fluxes are measured at two or more thermal wavelengths, so that the surface temperature can be constrained. A full spectrum, especially if it includes the peak in thermal emission, provides constraints on not just the temperature, but the temperature distribution, which in turn enables determination of the thermal inertia of the surface, even for measurements at a single epoch (e.g., Emery et al., 2006; Campins et al., 2009). Thermal inertia measurements help inform mission planners whether to expect a significant regolith cover or exposures of large boulders or bedrock, and it is also a critical parameter for modeling the effects of radiation pressure forces (i.e., Yarkovsky and YORP) on the orbit and spin state. Thermal emission spectra are also well suited for analyzing the mineralogy of the surface. This information can be especially critical for objects, like Bennu, whose visible and near-infrared reflectance spectra are featureless.

In this paper, we report thermal emission measurements of Bennu obtained with the Spitzer Space Telescope. The observations include thermal spectra (5.2–38 μm) at two longitudes and thermal photometric fluxes (3.6, 4.5, 5.8, 8.0, 16, and 22 μm) at ten longitudes. From these measurements, we place new constraints on the size, albedo, thermal inertia, and surface mineralogy of this asteroid, and we search for variations in these properties with rotation. Additionally, we perform a coma search using the thermal images.

2. Observations and data reduction

2.1. Overview of observations

The Spitzer Space Telescope (Werner et al., 2004) observed Bennu in three modes during the time period 3–9 May 2007. Since the rotation period had previously been well constrained by radar observations and ground-based lightcurve data, we were able to phase the observations for uniform longitude coverage. Thermal spectra from 5.2 to 38 μm were obtained with the Infrared Spectrograph (IRS; Houck et al., 2004) of opposite hemispheres of the body. Photometry at 16 and 22 μm was obtained with the IRS peak-up imaging (PUI) mode and at 3.6, 4.5, 5.8, and 8.0 μm with the Infrared Array Camera (IRAC; Fazio et al., 2004). The greater sensitivity of the imaging modes enabled shorter integration times. We made 11 observations of 10 fairly equally distributed

[2] http://www.minorplanetcenter.net/iau/NEO/TheNEOPage.html.

longitudes (repeating the first longitude as a consistency check) in order to search for rotational heterogeneities in thermal properties of the surface. Because Spitzer could only operate one science instrument at a time, it was not possible to obtain the PUI photometry simultaneously with the IRAC photometry. Instead, we planned the two sets of observations to be as close in time as possible, and rescaled the photometric data sets to a common viewing geometry, as described below (Section 2.3). The heliocentric distance during the observing period was 1.1238–1.1450 AU, the Spitzer-centric distance was 0.506–0.536 AU, and the phase angle was 63.5–61.7° (Table 1).

2.2. IRS spectroscopy

The thermal flux spectra were measured using the low-resolution ($\lambda/\Delta\lambda$ between 64 and 128) module of IRS. In this mode, IRS covers 5.2–38 μm in four segments: SL2 (5.2–8.5 μm), SL1 (7.4–14.2 μm), LL2 (14.0–21.5 μm), and LL1 (19.5–38.0 μm). The most diagnostic spectral features for silicate minerals occur near 10 μm. The spectral observations were therefore planned so as to obtain the highest S/N in the SL1 module. The IRS peak-up algorithm was used, in which the object is imaged and the center located for high-accuracy pointing to ensure that the object is placed in the center of the slit. Observations in each segment occurred with the object placed at about 1/3 and 2/3 of the slit length to ameliorate the effects of bad pixels and for later background subtraction. The reduction procedures we use herein for Spitzer/IRS spectra are described in detail in Emery et al. (2006) and Mueller et al. (2010). The steps include background subtraction, extraction to one-dimensional spectra, averaging multiple frames of each segment, and finally merging the four segments into a complete spectrum.

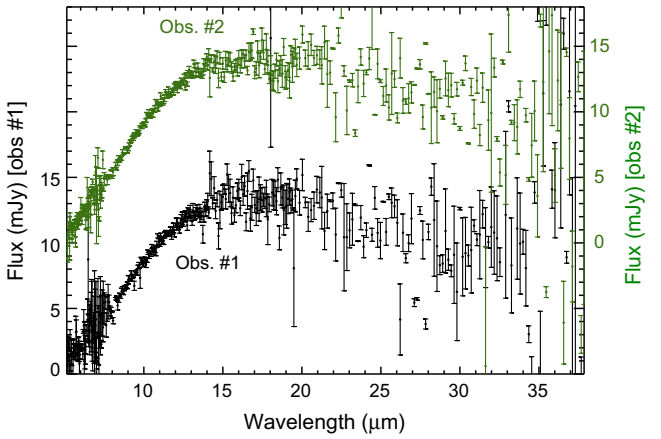

Fig. 1. Thermal flux spectra of Bennu measured by Spitzer/IRS. The scale for observation #1 (lower set of points) is on the left axis and the scale for observation #2 (upper set of points) is on the right. Observations were planned to obtain high sensitivity in the 8–14 μm region to search for silicate emissivity features.

The merging step can be somewhat difficult for low S/N data such as these. The absolute flux uncertainty in each module is ~5%; the telescope repoints to change modules (they are arranged at different places on the focal plane), introducing potential pointing errors between modules; and the image scale (pixel size) changes from SL to LL. All of these issues contribute to potential flux offsets between spectra from the different modules. Unfortunately, there is little (or, the cases of SL1 and LL2, no) overlap in wavelength between the modules, so getting the relative scaling correct is difficult. For high S/N data, extrapolation of the ends of

Table 1
Observing parameters.[a]

Mode	Date[b] (UT)	Time (UT)	Exposure time (s)				t_{AOR}[c] (min)	r[d] (AU)	Δ[d] (AU)	α[d] (°)
IRS spectra			SL2	SL1	LL2	LL1				
	3 May	21:39	960	600	1200	480	76.0	1.12678	0.50967	63.23
	3 May	23:46	960	600	1200	480	76.0	1.12707	0.51006	63.20
IRS PUI				Blue	Red					
AOR #1	3 May	00:00		30	30		4.23	1.12380	0.50564	63.52
AOR #2	3 May	04:40		30	30		4.23	1.12444	0.50650	63.46
AOR #3	4 May	11:11		30	30		4.23	1.12864	0.51222	63.05
AOR #4	3 May	09:55		30	30		4.23	1.12516	0.50748	63.39
AOR #5	4 May	07:40		30	30		4.23	1.12816	0.51155	63.10
AOR #6	3 May	10:44		30	30		4.23	1.12528	0.50762	63.38
AOR #7	3 May	02:32		30	30		4.23	1.12414	0.50611	63.48
AOR #8	3 May	20:08		30	30		4.23	1.12657	0.50938	63.25
AOR #9	3 May	03:29		30	30		4.23	1.12428	0.50629	63.47
AOR #10	3 May	08:10		30	30		4.23	1.12492	0.50716	63.41
AOR #11	3 May	08:33		30	30		4.23	1.12497	0.50722	63.40
IRAC			ch1	ch2	ch3	ch4				
AOR #1	8 May	16:24	60	60	60	60	3.93	1.14245	0.53224	61.78
AOR #2	8 May	16:46	60	60	60	60	3.93	1.14250	0.53232	61.78
AOR #3	8 May	17:14	60	60	60	60	3.93	1.14256	0.53241	61.77
AOR #4	8 May	17:39	60	60	60	60	3.93	1.14261	0.53250	61.77
AOR #5	8 May	18:06	60	60	60	60	3.93	1.14268	0.53259	61.76
AOR #6	8 May	18:27	60	60	60	60	3.93	1.14272	0.53266	61.76
AOR #7	8 May	18:59	60	60	60	60	3.93	1.14280	0.53278	61.75
AOR #8	8 May	19:22	60	60	60	60	3.93	1.14285	0.53285	61.75
AOR #9	8 May	19:50	60	60	60	60	3.93	1.14291	0.53295	61.74
AOR #10	8 May	20:16	60	60	60	60	3.93	1.14297	0.53304	61.73
AOR #11	8 May	20:39	60	60	60	60	3.93	1.14302	0.53312	61.73

[a] Date, time, r, Δ, and α given for beginning of observation.
[b] All observations were in 2007.
[c] Total length of clock time for the given observation, including overhead.
[d] r is heliocentric distance, Δ is Spitzer-asteroid distance, α is phase angle (Spitzer centered).

Table 2
IRS PUI fluxes.

AOR #	Blue (16 μm)		Red (22 μm)		IRAC AOR[a]	Blue, scaled[b]		Red, scaled[b]	
	Flux (mJy)	ΔFlux (mJy)	Flux (mJy)	ΔFlux (mJy)		Flux (mJy)	ΔFlux (mJy)	Flux (mJy)	ΔFlux (mJy)
1	14.61	0.31	13.62	0.45	4	13.20	0.28	12.35	0.41
2	13.92	0.31	13.18	0.46	5	12.61	0.28	11.98	0.42
3	14.17	0.31	13.33	0.47	6	13.11	0.29	12.37	0.44
4	13.85	0.31	13.07	0.46	7	12.58	0.28	11.92	0.42
5	13.88	0.32	12.91	0.47	7	12.81	0.29	11.95	0.44
6	14.75	0.31	13.65	0.46	9	13.40	0.29	12.45	0.42
7	14.73	0.31	13.57	0.46	10	13.35	0.28	12.35	0.41
8	13.50	0.30	12.76	0.45	11	12.38	0.27	11.75	0.41
9	13.97	0.31	13.19	0.46	2	12.65	0.28	12.00	0.42
10	14.18	0.32	13.89	0.46	3	12.88	0.29	12.67	0.42
11	14.47	0.31	13.72	0.46	4	13.14	0.28	12.52	0.42
Color corr[c]	0.984		0.997						

[a] IRAC observation that is closest in rotational phase.
[b] PUI fluxes rescaled to the observing geometry of IRAC measurements, as described in text.
[c] Aperture photometry has been divided by this factor.

each module to a common wavelength and validation by eye is generally quite effective. For low *S/N* data, however, such extrapolations have significant uncertainties, and the noise can hide mismatches. Changing the scaling between IRS modules changes the shape of the thermal flux curve, and thus has repercussions for the results of thermal modeling. In our thermal analysis, we place higher confidence in the results from the photometric data. For the IRS spectra presented here, we use the photometric data to help guide the scaling. The filters for the IRS and IRAC imaging modes cross between IRS spectral modules, so it is not possible to directly scale to the photometric data, but they do provide a useful starting point. For the thermal flux spectra shown in Fig. 1, the scaling factors are 1.00, 1.00, 1.03, and 1.08 for SL2, SL1, LL2, and LL1, respectively. Although no higher SNR data are available to test these factors, scaling uncertainties are included in the analysis of the spectral data. The absolute fluxes and spectral shapes of the observations of opposite hemispheres agree very well.

2.3. IRS peak-up imaging photometry

Along with its primary spectral capability, IRS also has two broad-band "peak-up" imaging (PUI) channels. The "blue" channel covers 13.3–18.7 μm, and the "red" channel covers 18.5–26.0 μm. Each channel has a rectangular field of view of 54 × 81 arcsec and a pixel scale of ~1.8 arcsec/pixel. The PUI channels operate at the diffraction limit of the optics. The point-spread full-width-at-half-maximum is about 3.8 and 5.3 arcsec for the blue and red channels, respectively. Each of the 11 observations in each channel consisted of a 5-point dither pattern of frames with integration times of 6 s. Scheduling issues precluded spacing the PUI observations evenly in time. Instead, we staggered the observations to get even coverage in longitude (rotational phase), allowing the observations to occur over several (8.2) rotation periods.

The Spitzer Science Center performs Standard calibrations (e.g., flat field, dark subtraction, bad-pixel identification, and flux calibration) using their data reduction pipeline.[3] We perform aperture photometry, including appropriate color and aperture corrections, on the basic calibrated data, which are flux calibrated to units of MJy/sr, using an aperture radius of 3 pixels for the blue channel and 4 pixels for the red. The measured fluxes are presented in Table 2 and Fig. 2.

[3] http://irsa.ipac.caltech.edu/data/SPITZER/docs/irs/irsinstrumenthandbook/home/

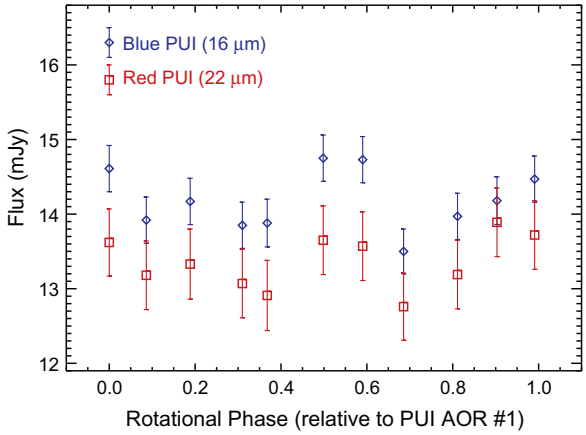

Fig. 2. Peak-up imaging photometry of Bennu from Spitzer/IRS. The diamonds are the blue (16 μm) channel and the squares are the red (22 μm) channel. Note that rotational phase 0.0 here corresponds to the start of the first PUI AOR, which is different than used throughout the remainder of the paper (where the rotational phase starts with the first IRAC AOR). (For interpretation of the references to color in this figure legend, the reader is referred to the web version of this article.)

The IRAC observations were conducted ~5 days after the PUI observations. In order to compile a photometric spectral energy distribution (SED) at each longitude, PUI observations are each matched with an IRAC observation taken at (nearly) the same rotational phase. The corresponding IRAC and PUI photometry sets are listed in Table 2. PUI fluxes are scaled for differences in observing geometry (heliocentric distance, Spitzer-centric distance, and solar phase angle). To calculate scale factors, model fluxes are calculated for each observing circumstance using thermal model parameters derived from fits to the IRS spectrum (Section 3.1.1). Scale factors, by which PUI fluxes are multiplied, are the ratio of the model fluxes for the IRAC observing geometry to those of the PUI observing geometry (see Fig. 3).

2.4. IRAC photometry

Bennu was also observed using all four channels of IRAC. IRAC obtains diffraction-limited images through filters with effective wavelengths of 3.550, 4.493, 5.731, and 7.872 μm and bandwidths of 0.750, 1.015, 1.425, and 2.906 μm. The four channels are referred to in this paper (and in much of the IRAC documentation) as ch1, ch2, ch3, and ch4 in order of increasing wavelength. Each channel

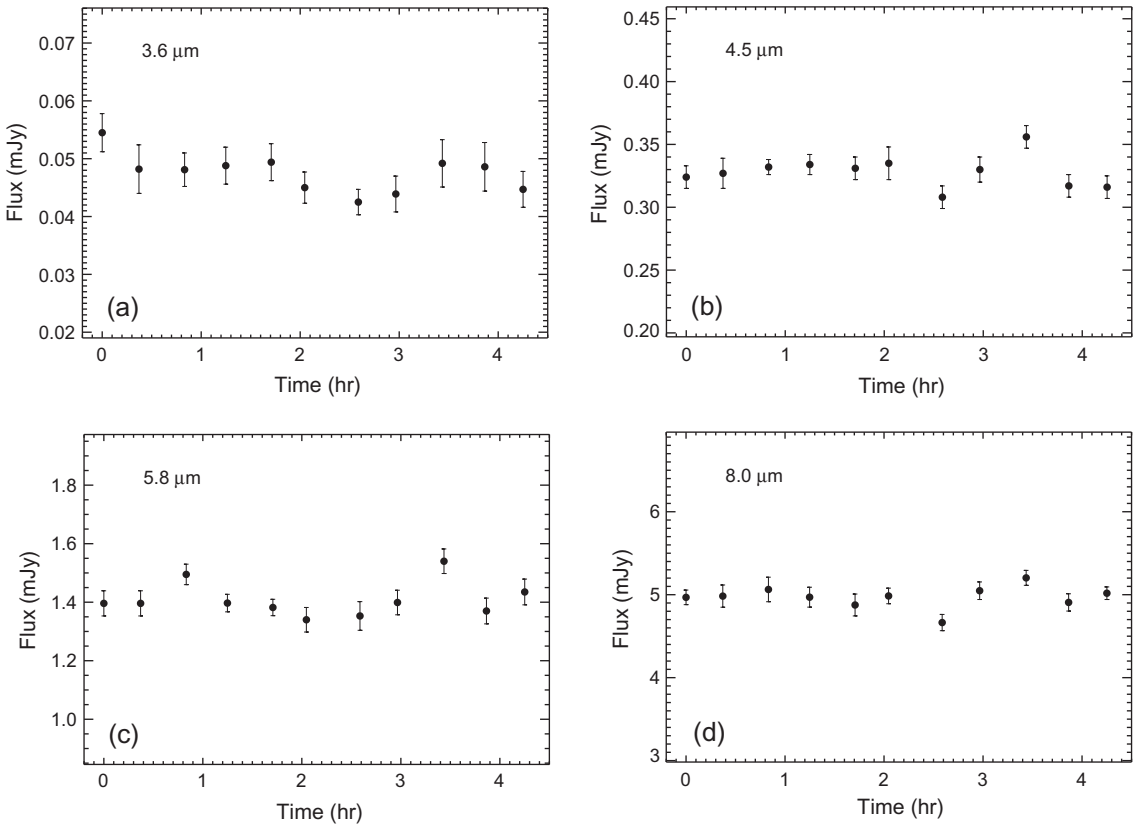

Fig. 3. IRAC imaging photometry from Spitzer. All IRAC data were taken within one rotation period of Bennu (~4.297 h). (a) 3.6 μm, (b) 4.5 μm, (c) 5.8 μm, (d) 8.0 μm. The *x*-axis gives the time from the start of the first IRAC AOR.

has a FOV of 5.2 × 5.2 arcmin and pixel scale of ~1.2 arcsec (during these observations, the angular size of Bennu was about 0.0014 arcsec). The detectors for ch1 and ch2 are InSb arrays, whereas ch3 and ch4 use SiAs detectors. The detector response, including artifacts, therefore differs between the shorter and longer wavelength channels. The optics of IRAC are designed such that ch1 and ch3 are paired for simultaneous observations, and ch2 and ch4 are likewise paired. The telescope is repointed to switch between the two (paired) FOVs. Each of the 11 observations in each channel consisted of a 5-point dither pattern of frames with integration times of 12 s. In this case, unlike PUI, the observations were spread fairly evenly during a single ~4.29 h rotation of the asteroid.

The data processing and calibration pipeline[4] run by the Spitzer Science Center performs all basic calibration (e.g., dark subtraction, flat field correction, absolute flux calibration). The output of the data pipeline includes basic calibrated data (BCD) – 2D images in units of MJy/sr. Several well-characterized artifacts (e.g., stray light, saturation, column pulldown) are corrected in an extension of the pipeline and presented as corrected basic calibrated data (CBCD). Performing aperture photometry on the CBCD frames, after a few extra processing steps, yields the fluxes presented here.

The 11 IRAC observations are separated by ~20 to 30 min in time, during which Bennu moves about an arcminute or so across the FOV. Adjacent observations (in time) are therefore used as background frames for each other. To create a background frame, the dithered target frames are averaged (omitting outliers) after shifting to a common pointing. The average background image (which differs for each of the 11 observations) is subtracted off of each CBCD frame before the photometric calculation. Most of the ch1 observations contained latent images from previous observations of bright stars. These are removed by median-combining the dithered frames in array coordinates, and then subtracting this latent image from the data frames. The ch3 frames all contain a gradient across the array, which is removed by calculating a row-by-row and column-by-column median and subtracting from the frame. The latent image correction for ch1 is significant for some frames (depending on whether Bennu fell on a latent image or not), but the gradient correction for ch3 does not significantly affect the final flux. We also apply the corrections provided by the Spitzer Science Center for variations in the pixel solid angle across the arrays and for array location-dependent photometric variations.

The images are converted to units of mJy/pixel before performing aperture photometry. We use 2- and 3-pixel radius apertures with background annuli of 2–6 and 3–7 pixels, respectively. Corresponding aperture corrections are given in the IRAC instrument handbook for each channel. Color corrections (see Table 3) are calculated by integrating the model thermal flux weighted by the known filter functions. The model thermal flux is computed using the Near-Earth Asteroid Thermal Model (NEATM; Harris, 1998) and parameters derived by fitting the IRS spectrum (see Section 3.1.1). Bennu is identified on each frame by predicting the pixel position from the known ephemeris and the pointing keywords in the image header. Bennu is bright enough to see in each frame. We use a centroiding algorithm to calculate the sub-pixel position of the point response function (PRF) maximum, which we use to apply

[4] http://irsa.ipac.caltech.edu/data/SPITZER/docs/irac/iracinstrumenthandbook/home/

Table 3
IRAC fluxes.

AOR #	ch1 (3.6 μm)		ch2 (4.5 μm)		ch3 (5.8 μm)		ch4 (8.0 μm)	
	Flux (mJy)	ΔFlux (mJy)	Flux (mJy)	ΔFlux (mJy)	Flux (mJy)	ΔFlux (mJy)	Flux (mJy)	ΔFlux (mJy)
1	0.0545	0.0033	0.324	0.009	1.396	0.043	4.968	0.044
2	0.0482	0.0042	0.327	0.012	1.396	0.043	4.983	0.067
3	0.0481	0.0029	0.332	0.006	1.495	0.035	5.063	0.074
4	0.0488	0.0032	0.334	0.008	1.397	0.030	4.970	0.060
5	0.0494	0.0032	0.331	0.009	1.382	0.028	4.876	0.066
6	0.0450	0.0027	0.335	0.013	1.340	0.042	4.985	0.047
7	0.0425	0.0022	0.308	0.009	1.353	0.049	4.664	0.049
8	0.0439	0.0031	0.330	0.010	1.399	0.042	5.048	0.053
9	0.0492	0.0041	0.356	0.009	1.540	0.042	5.203	0.045
10	0.0486	0.0042	0.317	0.009	1.370	0.044	4.907	0.052
11	0.0447	0.0031	0.316	0.009	1.435	0.044	5.018	0.038
Color corr.[a]	1.132		1.067		1.031		1.002	

[a] Aperture photometry has been divided by this factor, which corrects the photometric calibration for the spectral shape of the source.

the pixel-phase-dependent photometric correction for ch1 and ch2 as described in the IRAC instrument handbook. For each observation, the fluxes from the 5 dithered frames are averages, omitting outliers (>5σ). The reported uncertainties are 1σ and fold together in quadrature the photometric uncertainties for each frame and the statistical variation among the dithered frames.

3. Analysis

3.1. Thermal modeling

The thermal spectroscopic and photometric fluxes measured for Bennu comprise a significant dataset that contains information on physical properties such as size, albedo, thermal inertia, and surface roughness. Unraveling the effects of these properties and appropriately assessing uncertainties and trade-offs is complex, and few objects have been observed as comprehensively in the thermal infrared. We therefore begin the analysis of Bennu with relatively simple techniques that are applied to large sets of asteroids, then increase the complexity and specificity. The goal of this approach is to place the current results in context with broader asteroid data sets while also providing greater insight into the reliability of the final results.

For all levels of complexity discussed below, the general scheme for modeling disk integrated thermal emission is the same. In this scheme, we attempt to match the measured flux by varying the temperature distribution across the surface, calculating the flux at each location using the Planck function, then integrating over the portion of the surface visible to the observer. Mathematically,

$$F_\lambda = \frac{1}{\Delta^2}\int \varepsilon_\lambda B(\lambda,T)\cos\theta_e \mathrm{d}A, \quad (1)$$

where Δ is the observer-asteroid distance, ε_λ is the spectral emissivity, dA is incremental surface area, $B(\lambda,T)$ is the Planck function, T is temperature, θ_e is the emission angle, and λ is wavelength. Complexity enters the calculation in terms of the temperature distribution inserted into the Planck function to compute the flux from each point on the surface. For a spherical body of uniform emissivity, the flux equation becomes

$$F_\lambda = \frac{R_{eff}^2}{\Delta^2}\varepsilon\iint B(\lambda,T)\cos\theta_e \sin\theta_e d\theta_e \mathrm{d}\phi. \quad (2)$$

R_{eff} is the radius of the spherical body (also called the effective radius, which is half the effective diameter; D_{eff}) and ϕ is the azimuthal angle around the axis pointing toward the observer. Bolometric emissivities of silicates at asteroidal temperatures are generally 0.90–0.95, justifying the assumption of uniform emissivity.[5] The temperature distribution is varied to match the spectral shape, and R is adjusted to fit the absolute flux level. A measurement or estimate of the visible flux is required in order to constrain the albedo. Throughout this work, we use the measurement of visible absolute magnitude from Hergenrother et al. (2013) to constrain the albedo (see Section 3.1.1).

3.1.1. Near-Earth Asteroid Thermal Model (NEATM)

A reasonable starting point for thermal modeling of asteroids assumes a spherical shape and considers the surface to be in instantaneous equilibrium between incoming solar insolation and outgoing thermal radiation; in other words, the thermal inertia is zero. Assuming a single blackbody is simpler, but is not realistic in that it does not adequately reproduce the thermal continuum (e.g., Emery et al., 2006), since the visible portion of any unresolved asteroid will be comprised of a mix of surface temperatures. The sub-solar temperature in this case is given by

$$T_{ss} = \left[\frac{S_o}{r_{AU}^2}\frac{(1-A_B)}{\eta\varepsilon\sigma}\right]^{\frac{1}{4}}, \quad (3)$$

where S_o is the solar flux at 1 AU (1366 W m^{-2}; Frölich, 2009), A_B is the bolometric Bond albedo, r_{AU} is the heliocentric distance in AU, ε is the bolometric emissivity (taken throughout this paper to be 0.9, a typical value for rocky material[5]), σ is the Stefan–Boltzmann constant, and η is an empirical factor called the beaming parameter, which is used to adjust the temperature to match the observed flux (e.g., Lebofsky and Spencer, 1989). Since the body is assumed to be spherical and Lambertian, the temperature falls off as $T(\theta_i) = T_{ss}\cos^{1/4}\theta_i$, where θ_i is the incidence or solar zenith angle, and is assumed to be zero on the nightside. The thermal flux is integrated over the hemisphere visible to the observer. This model is referred to as the Near-Earth Asteroid Thermal Model (NEATM) and is discussed in detail in Harris (1998).

Application of the NEATM to the measured IRS spectra produces a good fit to the data (Fig. 4). The resulting estimates of the asteroid physical parameters are listed in Table 5. A χ^2 minimization algorithm based on the Brent (1973) implementation of parabolic interpolation (Press et al., 1992) is used to find the size and T_{ss} that

[5] The bolometric emissivity is the average spectral emissivity, weighted by the thermal continuum flux spectrum. At the relevant temperatures for asteroids, the wavelength range that contributes most to this average is ~8 to ~40 μm. This wavelength range encompasses the strong Si–O stretch and bend fundamental absorptions common to all silicate materials. The high imaginary indices of refraction throughout this wavelength range lead to spectral emissivities that are generally between 0.8 and 1.0 (e.g., Salisbury et al. 1992; Christensen et al., 2000).

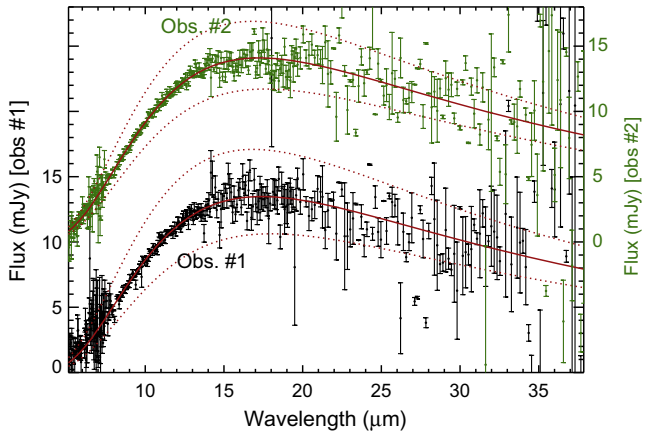

Fig. 4. NEATM fits to IRS data. The scale for observation #1 (lower set of points) is on the left axis and the scale for observation #2 (upper set of points) is on the right. Solid curves are the best-fit thermal continua, and the dashed curves illustrate the full envelopes described by the combined parameter uncertainties in Table 5.

most closely reproduce the measured flux. At each minimization step, the geometric albedo is calculated from the radius using the absolute magnitude (H_v): $p_v = (D_o/D_{eff})^2 10^{-0.4Hv}$, where D_o is taken to be 1329 km and H_v for Bennu is 20.51 ± 0.10 (Hergenrother et al., 2013). The Bond albedo is calculated as $A_B = p_v q$, where q is the phase integral (0.367 ± 0.045), which in turn is computed by integrating the linear phase curve with $\beta = 0.040 \pm 0.03$ mag/deg (Hergenrother et al., 2013). Uncertainties in fit parameters are found by fitting the data at the extremes of the relative and absolute uncertainties. The two IRS observations, which were timed to observe opposite hemispheres of Bennu, agree extremely well with each other, indicating that a longitudinal hemispherical dichotomy in albedo or thermal properties probably does not exist. The NEATM-derived effective diameter ($D_{eff} \sim 612$ m) is significantly larger than that measured by radar (492 ± 20 m; Nolan et al., 2013). NEATM is known to overestimate sizes of objects measured at large phase angles, such as the ~62° at which our data were measured (e.g., Wolters and Green, 2009), as discussed in more detail in Section 4.1.

The beaming parameter (η) is a non-physical factor in the NEATM that is used to adjust the sub-solar point temperature as a proxy for more complex effects. The two main physical parameters affecting η are macroscopic surface roughness, which lowers η, and thermal inertia, which raises η. Values of $\eta > 1$ are generally consistent with elevated thermal inertias (Delbó et al., 2007), though η also generally increases with phase angle of observation (e.g., Wolters et al., 2008). The large beaming parameter derived for Bennu using this method (Table 5) is therefore suggestive of a thermal inertia higher than found for the Moon or large asteroids.

We also conduct a search for local- to regional-scale thermal heterogeneities on the surface. When combined, the IRAC and IRS

Table 4
PUI fluxes interpolated to IRAC rotational phases.

IRAC AOR #	Rotational phase[a]	Blue (16 μm)		Red (22 μm)	
		Flux (mJy)	ΔFlux (mJy)	Flux (mJy)	ΔFlux (mJy)
1	0.0000	12.49	0.28	11.85	0.41
2	0.0864	12.69	0.29	12.09	0.40
3	0.1937	12.97	0.28	12.62	0.42
4	0.2905	13.00	0.28	12.23	0.40
5	0.3973	12.85	0.29	12.17	0.42
6	0.4761	13.00	0.28	12.28	0.43
7	0.6020	12.70	0.28	11.94	0.42
8	0.6901	13.08	0.30	12.18	0.44
9	0.7994	13.38	0.28	12.40	0.42
10	0.8992	12.87	0.27	12.05	0.41
11	0.9892	12.47	0.28	11.83	0.42

[a] Rotational phase relative to 1st IRAC astronomical observation request (AOR; the Spitzer term for each planned observation), calculated from the start time of each AOR.

Table 5
Results from NEATM fits.

Observation	Rot. phase[a]	D_{eff}[b] (m)	ΔD_{eff} (m)	T_{ss} (K)	ΔT_{ss} (K)	η	$\Delta\eta$	p_v[b]	Δp_v[c]
IRS #1	0.30–0.57	612	46[d]	339	11[d]	1.57	0.21[d]	0.029	0.005[d]
IRS #2	0.79–0.06	613	42[d]	341	10[d]	1.54	0.19[d]	0.029	0.005[d]
IRAC+PUI 1	0.0000	595	8	339.3	1.6	1.53	0.03		
IRAC+PUI 2	0.0864	601	9	338.4	1.7	1.55	0.03		
IRAC+PUI 3	0.1937	604	7	339.4	1.1	1.53	0.02		
IRAC+PUI 4	0.2905	602	8	338.5	1.4	1.54	0.03		
IRAC+PUI 5	0.3973	599	8	338.2	1.6	1.55	0.03		
IRAC+PUI 6	0.4761	610	9	336.9	1.8	1.57	0.03		
IRAC+PUI 7	0.6020	598	9	336.1	1.6	1.59	0.03		
IRAC+PUI 8	0.6901	609	9	337.9	1.6	1.56	0.03		
IRAC+PUI 9	0.7994	601	9	341.5	1.7	1.49	0.03		
IRAC+PUI 10	0.8992	605	8	337.1	1.4	1.57	0.03		
IRAC+PUI 11	0.9892	599	7	339.2	1.4	1.53	0.03		
Average		*602*	*10*					*0.030*	*0.003*

[a] Rotational phase relative to 1st IRAC AOR, calculated from the start time of each AOR. Repeated in Tables 6 and 7 for ease of reference.
[b] Effective diameter fits from NEATM at large phase angles are known to be over-estimates and are shown here only for comparison to other NEATM results. Likewise, the p_v values from NEATM are under-estimates (e.g., Wolters and Green, 2009).
[c] Δp_v includes uncertainty from D_{eff} and from H_v ($\Delta H_v = 0.10$; Hergenrother et al., 2013).
[d] Uncertainties here are from range of good fits to the nominal spectral scaling. IRS results have additional uncertainty from relative scaling of the four modules of 11 m ΔD_{eff}, 0.002 in p_v, 8 K in T_{ss} and 0.15 in η (1σ, from a Monte Carlo analysis). These additional uncertainties most strongly affect the temperature-related quantities (T_{ss} and η), since the relative scaling changes the shape of the thermal flux spectrum.

PUI photometry comprise thermal spectral energy distributions (SEDs) from 3.6 to 22 μm at 10 different (and 1 repeated) rotational phases. Other small bodies (e.g., Itokawa, Eros, Hartley 2, Tempel 1) exhibit a mix of blocky and finer-grained terrains (ponds, seas, flows, smooth regions). We expect such units to have different thermal properties, which must be expressed in their thermally emitted flux. Even after scaling for different observing geometry, as described in Section 2.3, there are still slight rotational offsets between the PUI and IRAC observations. The difference in rotational phase ranges from 4° of rotation to 17°, with an average difference of 10°. To account for lightcurve effects due to these differences in rotational phase, the PUI fluxes are linearly interpolated to the rotational phase of the corresponding IRAC observation (Table 4).

To search for rotational variation, we fit NEATM to the photometric SEDs at each rotational phase. Resulting parameters are listed in Table 5, and Fig. 5 shows the model fits to each of the photometric SEDs. Uncertainties in fit parameters are computed from a Monte Carlo analysis where the fluxes are randomly varied according to listed uncertainties and the standard deviation of parameters is derived from the range of model results. The best-fit D_{eff} is fairly constant with rotation, varying by at most 15 m (Fig. 6), which is within the 1σ uncertainties and is comparable to the change in cross-sectional area with rotation from the radar shape model (Nolan et al., 2013). T_{ss}, the other quantity directly fit by NEATM, varies more significantly relative to the uncertainties in the fit, though the magnitude of the variation is still only ~5 K (Fig. 6).

The geometric albedo (p_v) and the beaming parameter (η), quantities typically discussed with respect to NEATM, are derived from D_{eff} and T_{ss}. If we were to use a constant H_v to calculate p_v, the rotational signature would be the inverse of that seen for D_{eff}. However, visible lightcurve measurements clearly show a variation in brightness with rotation (Hergenrother et al., 2013). It is tempting to try scaling H_v for the rotational phase of each photometric observation, then calculate a p_v from the NEATM size and scaled

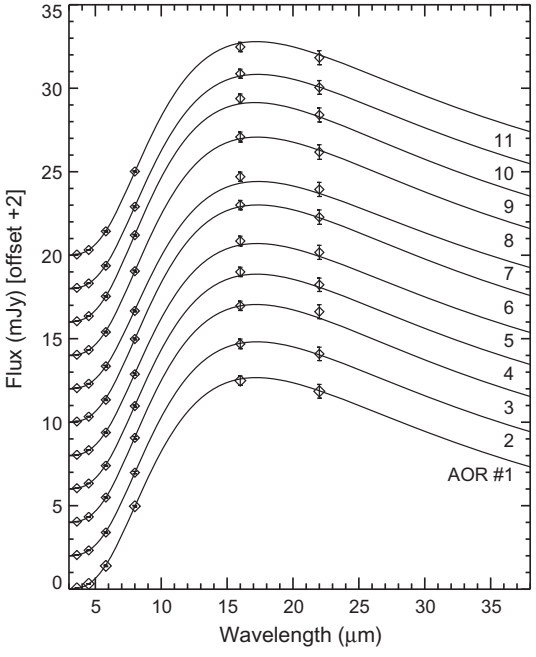

Fig. 5. NEATM fits to photometric SEDs. Open diamonds are Spitzer IRAC and PUI data. Solid lines are NEATM fits. Fluxes from AOR #1 are shown at measured fluxes, and fluxes from the other AORS are offset by increments of 2 mJy. Parameters for the NEATM fits are listed in Table 5.

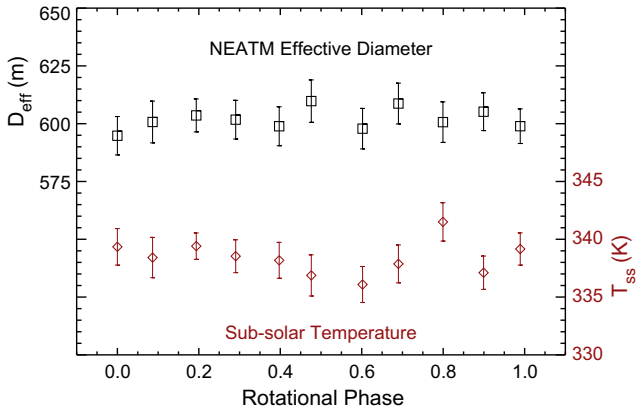

Fig. 6. Effective diameter (squares) and sub-solar temperature (diamonds) from NEATM fits to the photometric data. These are the two parameters directly fit by NEATM. The effective diameter (i.e., cross-sectional area) is relatively constant with rotation, but T_{ss} shows variation that is marginally statistically significant.

H_v in order to search for albedo variations. Unfortunately, the simple relationship among D_{eff}, p_v, and H_v noted above is strictly valid only for spherical objects. Therefore, without additional information, the NEATM analysis cannot determine whether the albedo varies across the surface. Table 5 includes an estimate of p_v from the average NEATM diameter from the photometric observations, for comparison to the results from the spectral observations. Since p_v is very low, η effectively only depends on T_{ss}, and its rotational profile mirrors that of T_{ss} (Fig. 6).

3.1.2. Thermophysical models

Determination of the thermal inertia is important for understanding the nature of Bennu's surface. As described above, the beaming parameter is at best a proxy for thermal inertia. We can improve our knowledge of thermal inertia for Bennu using thermophysical modeling because: (a) important rotational parameters (period, spin-pole orientation) are known, and (b) the thermal data are high quality and cover a broad spectral range. The thermophysical model (TPM) employed here is described in Emery et al. (2006) and the roughness implementation by Emery et al. (1998), both of which are broadly similar to the model described by Spencer (1990). Briefly, we model one-dimensional heat flow into the surface, assuming thermal properties that are constant with depth and temperature. Spherical section craters serve as macroscopic (larger than the thermal skin-depth, but otherwise of arbitrary size) roughness elements to incorporate shadowing, self-heating, multiple scattering, and visibility-shadowing. Roughness is characterized by an RMS surface slope, but the implementation requires two parameters: the crater half-opening (γ) and the fractional coverage of craters (f). Because thermal inertia and roughness are now explicitly included, η is not used in this model. In this step, we continue to assume that the asteroid is spherical.

The procedure for constraining thermal inertia and asteroid radius is similar to that used in Section 3.1.1 to constrain η and size. For a given value of thermal inertia, we vary radius (assuming a spherical shape) to fit the observation (i.e., minimizing χ^2). We step through a grid of thermal inertia from 0 to 2500 J m^{-2} s$^{-1/2}$ K^{-1}, eventually finding the combination of thermal inertia and radius that produces the global best-fit model (minimum χ^2). The best-fit thermal inertia depends somewhat on assumed surface roughness (Fig. 7), but falls around 400 J m^{-2} s$^{-1/2}$ K^{-1} for the photometric data (Table 6) for a surface with RMS surface slope of 20° (γ = 53°, f = 0.77). Best-fit thermal inertias from the spectral data are slightly higher, but the uncertainties are also significantly

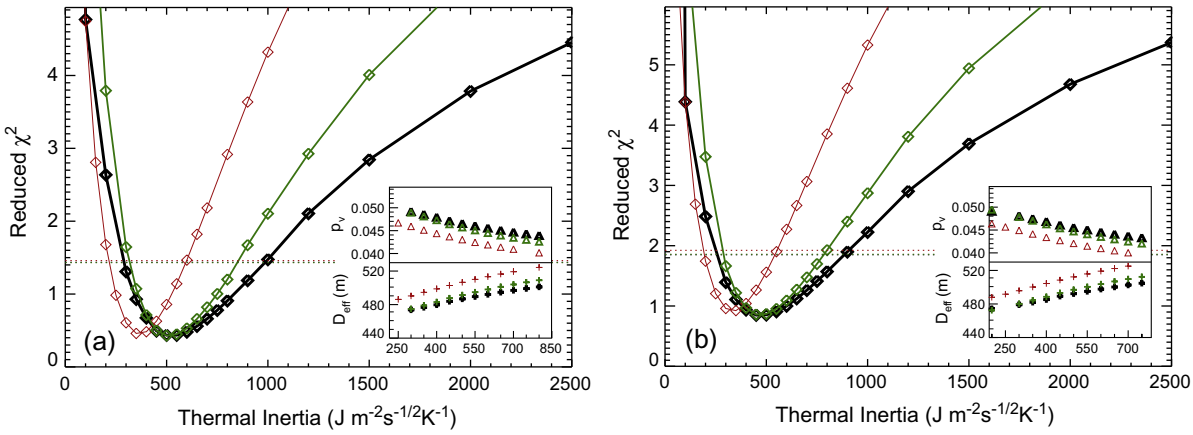

Fig. 7. Goodness-of-fit for three different surface roughness values for the two spectral (IRS) observations. (a) Observation #1. (b) Observation #2. Diamonds and solid lines illustrate the reduced-χ^2 versus thermal inertia. The different curves are different values of surface roughness: red/thin is a smooth surface, black/thick is an extremely rough surface (RMS surface slope 66°), and green/medium-thick is the nominal surface roughness (20°). Dashed lines mark $\chi^2_{min}+1$, which is a good measure of 1σ uncertainties. The insets show effective diameter (lower frame; plus symbols) and geometric albedo (upper frame; open triangles) for each thermal inertia near the minimum of the χ^2 curves (x-axis is thermal inertia). (For interpretation of the references to color in this figure legend, the reader is referred to the web version of this article.)

Table 6
Results from spherical TPM fits.

Observation	Rot. phase[a]	D_{eff} (m)	ΔD_{eff} (m)	Γ (J m^{-2} s$^{-1/2}$ K^{-1})	$\Delta\Gamma$[b] (J m^{-2} s$^{-1/2}$ K^{-1})	p_v	Δp_v[c]
IRS #1	0.30–0.57	492	+18 −16	516	+332 (333) −199 (205)	0.046	0.005
IRS #2	0.79–0.06	494	+19 −15	471	+312 (313) −186 (191)	0.045	0.005
IRAC+PUI 1	0.0000	477	9	377	+57 (59) −50 (60)		
IRAC+PUI 2	0.0864	482	9	395	+70 (72) −58 (67)		
IRAC+PUI 3	0.1937	488	9	380	+44 (47) −40 (52)		
IRAC+PUI 4	0.2905	484	9	393	+54 (57) −47 (58)		
IRAC+PUI 5	0.3973	482	10	403	+59 (62) −53 (64)		
IRAC+PUI 6	0.4761	488	10	433	+82 (84) −67 (77)		
IRAC+PUI 7	0.6020	479	9	428	+71 (73) −59 (69)		
IRAC+PUI 8	0.6901	487	9	401	+65 (68) −55 (65)		
IRAC+PUI 9	0.7994	488	8	342	+48 (51) −43 (53)		
IRAC+PUI 10	0.8992	485	9	419	+65 (67) −54 (65)		
IRAC+PUI 11	0.9892	480	9	385	+58 (60) −50 (61)		
Average		*484*	*10*	*396*	*32*	*0.0471*	*0.0047*

[a] Rotational phase relative to 1st IRAC AOR, calculated from the start time of each AOR. Repeated from Table 5 for ease of reference.
[b] Primary $\Delta\Gamma$ is region where $\chi^2 < \chi^2_{min}+1$ for nominal roughness case (RMS = 20°). Values in parentheses include surface roughness contribution, taking the RMS = 0° and 66° surfaces as 3σ cases. The effects on ΔD_{eff} and Δp_v are negligible.
[c] Δp_v includes uncertainty from D and from H_v ($\Delta H_v = 0.10$; Hergenrother et al., 2013).

larger. Thermal inertia uncertainties for a given surface roughness are assessed by noting that $\chi^2-\chi^2_{min}=1$ corresponds to 1σ in the fit parameter (and $\chi^2-\chi^2_{min}=9$ to 3σ; Press et al., 1992; Bevington and Robinson, 2003). Uncertainties from surface roughness are added in quadrature, taking RMS = 0° and RMS = 66° (γ = 90°, f = 1.0) as 3σ ranges in roughness. Parameter results from thermophysical fits are listed in Table 6. The derived (spherical) D_{eff} is now in better agreement with the radar measurements, essentially due to the inclusion of nightside emission, and the albedo is correspondingly higher than for the NEATM fits, as expected. D_{eff} from the spherical thermal model is still a bit smaller than that from the radar shape at the same viewing geometry (484 m vs 496 m). This can be understood in terms of shape effects in thermal modeling, as discussed below (Sections 3.1.3 and 4.1).

Our analyses reveal no gross hemispherical differences in thermal inertia. The models of the two IRS spectra again agree with each other within uncertainties. Fits to the photometric SEDs show some hints of small variation in thermal inertia (Fig. 8), particularly indicating a low thermal inertia region near rotational phase of 0.8. D_{eff} (i.e., cross-sectional area) is fairly constant with rotation, though variation on the order of the uncertainties is apparent (Fig. 8). D_{eff} as a function of rotational phase calculated from the

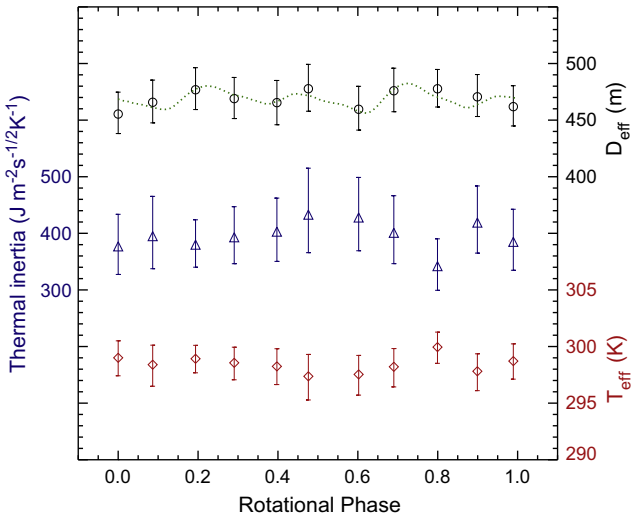

Fig. 8. Parameters from TPM fits as a function of rotation with a spherical shape model and nominal roughness (RMS = 20°; $\gamma = 53°$, $f = 0.77$). Thermal inertia is plotted as triangles (left axis), effective temperature as diamonds (lower right axis), and effective diameter as circles (upper right axis). The dotted line is the effective diameter ($D_{eff} = \mathrm{sqrt}[A_{cs}/\pi]$) from the radar shape model, scaled by 0.976. These results suggest a region of low thermal inertia and slightly elevated temperature at a rotational phase of 0.8. The measured relative variation in cross-sectional area with rotation is well described by the radar shape model.

radar shape model is overplotted in Fig. 8. The phasing of the observations relative to the shape model is from fitting the thermal lightcurve (see Section 3.1.3). The rotational variation in the thermally derived size is in very good agreement with the shape model. The thermal results thereby support the assumption of constant albedo used in the determination of the shape model (Nolan et al., 2013). If the shape determination had misinterpreted an albedo spot in terms of shape, we would expect a discrepancy between the thermal size and the shape model. A similar analysis with NEATM is not as robust, because that simple model ignores thermal emission from the nightside.

The TPM fits to the photometric SEDs also reveal a slightly higher temperature near rotational phase 0.8 (Fig. 8). The effective temperature (T_{eff}) shown in Fig. 8 is the temperature of a blackbody with the same wavelength-integrated (bolometric) flux as the model. The NEATM analysis also suggests this elevated temperature. The spherical TPM interprets the higher temperature as a lower thermal inertia. If real, the most straightforward interpretation of a lower thermal inertia would be a smaller average grain size (e.g., a dustier region). However, shape effects could also lead to temperature differences, particularly when analyzed with a spherical model, as done in this section. Differences in surface roughness could also lead to apparent temperature difference. Both of these possibilities are addressed in the next section.

3.1.3. Shape

To increase our thermal model to the next level of fidelity, we incorporated the radar-derived shape model. So far, we have assumed Bennu is spherical. However, the shape of this asteroid is known to a resolution of 7.5 m, derived by folding together radar and visible lightcurve measurements (Nolan et al., 2013). Incorporating that shape into the thermal model enables a greater focus on the thermal properties of the surface rather than size and shape. The modeling approach is basically the same as described above, except that now, instead of distributing the facets on a sphere,

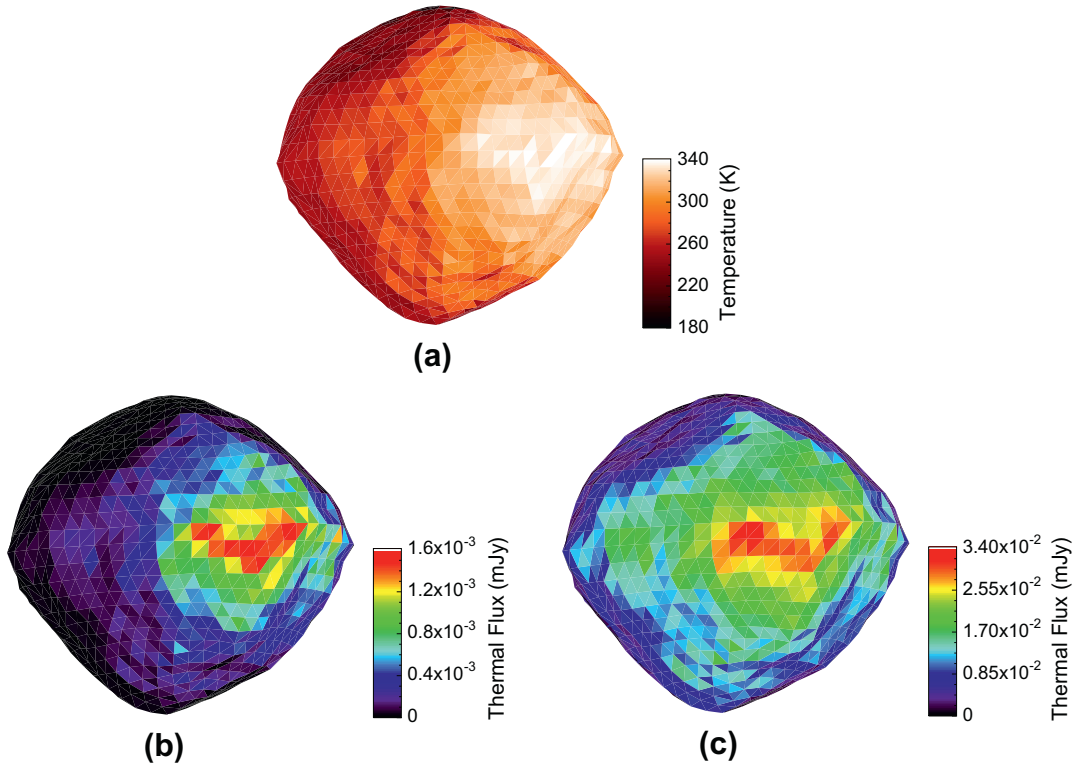

Fig. 9. Thermal model images incorporating the radar shape. (a) Temperature. (b) Thermal flux in IRAC ch2 (4.5 μm). (c) Thermal flux in the red (22 μm) IRS PUI channel. All images are for a smooth surface with $\Gamma = 250$ J m^{-2} s$^{-1/2}$ K^{-1}. (For interpretation of the references to color in this figure legend, the reader is referred to the web version of this article.)

the illumination and viewing geometries and shadowing of the individual surface facets are calculated from the shape model.

Inclusion of the shape model allows us to develop more detailed flux estimates. An example temperature image (for a smooth surface, thermal inertia = 250 J m^{-2} s$^{-1/2}$ K^{-1}, and the observing geometry of the IRAC observations) along with thermal flux images at 4.5 and 22 μm are shown in Fig. 9. The flux model images illustrate that different wavelengths do not necessarily sample the same portion of the surface. Shorter wavelengths, on the Wien side of the thermal peak, preferentially sample the hottest parts of the surface. Longer wavelengths, on the other hand, show the contribution of cooler facets, and the observed flux is more uniformly distributed across the surface. For surfaces viewed at phase angles $\lesssim$90°, increased surface roughness also tends to, on average, increase the temperatures of visible surface facets, so the effects of surface roughness are also most apparent at shorter wavelengths (Emery et al., 1998).

Since size is inherently part of the shape model, it is not an independent parameter in this analysis. We take the albedo to be the value derived from previous steps (which agrees with the value derived using H_v and the radar size). Information we do not know beforehand includes the thermal inertia, the surface roughness, and the rotational phase (mapped to the shape model) of each observation. We therefore compute thermal model fluxes for a range of thermal inertias (0–2500 J m^{-2} s$^{-1/2}$ K^{-1}, in steps of 50), surface roughness (RMS slope = 0°, 20°, 66°), and at every 1 degree of rotation.

Incorporation of the shape model results in a substantial improvement to our thermal inertia determination. A simultaneous χ^2 minimization of all of the photometric data finds a rotational offset between the (arbitrarily chosen) radar zero longitude and the (arbitrarily chosen) start time of the photometric observations of ~74° (Fig. 10). The thermal inertia values reported in Table 7 are the minimum of a polynomial fit to χ^2 vs thermal inertia at each rotational phase (after shifting by 74°). The best-fit thermal inertia is somewhat lower than estimated using a spherical shape. The lower thermal inertia is most likely a result of Bennu's oblateness. The radar images reveal an equatorial diameter 535 and 565 m in the long and short dimensions, respectively, and polar diameter 508 m (Nolan et al., 2013). As a result, the non-equatorial facets are, on average, more tilted relative to both the Sun and observer than they would be for a sphere, leading to lower temperatures and fluxes. The thermal model runs using a spherical shape would compensate for the different tilts with a slightly higher thermal inertia and slightly smaller effective diameter. Thermal inertia derived using the radar shape is therefore considered to be more accurate.

When taking shape into consideration in the thermal model, a variation of thermal inertia with rotational phase is apparent (Fig. 11). The magnitude of this variation is similar to that seen in results using a spherical shape. The rotational profile, on the other hand, is very different, indicating lows in thermal inertia near rotational phases of 0.4 and 0.9. When assuming a uniform surface roughness, the thermal inertia variation would be difficult to discount. However, the highest thermal inertias assuming a smooth surface overlap the lowest thermal inertias assuming a rough surface. It is therefore possible that the surface heterogeneity is in (macroscopic) surface roughness rather than thermal inertia.

We use the photometric data to test the fidelity of shape and albedo constraints. These data can be visualized as a set of thermal lightcurves at six different wavelengths. Fig. 12 illustrates these lightcurves at three wavelengths, with corresponding model thermal lightcurves overplotted for comparison. In these plots, the thermal models have been interpolated from the grid of 50 J m^{-2} s$^{-1/2}$ K^{-1} over which they were run to the measured values given in Table 7 (and shown in Fig. 12) at each rotational phase. The model fluxes match the shapes of the measured lightcurves quite well, providing confidence in the radar-derived shape and assumption of uniform albedo.

Using the best available information on the shape and spin-state of Bennu, we find a thermal inertia of ~310 J m^{-2} K^{-1} s$^{-1/2}$ and a fairly longitudinally homogeneous surface. These results are discussed further in Section 4. We started this section by noting that the radar shape includes size. That size does, however, have an uncertainty associated with it. We repeated the analyses allowing the overall radar size to vary within the uncertainties quoted by Nolan et al. (2013). We find that the nominal radar size does give the best fit to the Spitzer data and that the contribution to the final thermal inertia uncertainties (1σ) from uncertainty in radar size is ±20 J m^{-2} K^{-1} s$^{-1/2}$ (see Section 4).

3.2. Emissivity spectra

The mid-infrared (MIR) spectral region, including the range 5.2–38 μm observed spectrally with IRS on Spitzer, contains diagnostic vibrational bands of many minerals, particularly silicates. MIR emissivity spectra of silicate-rich surfaces are often difficult to

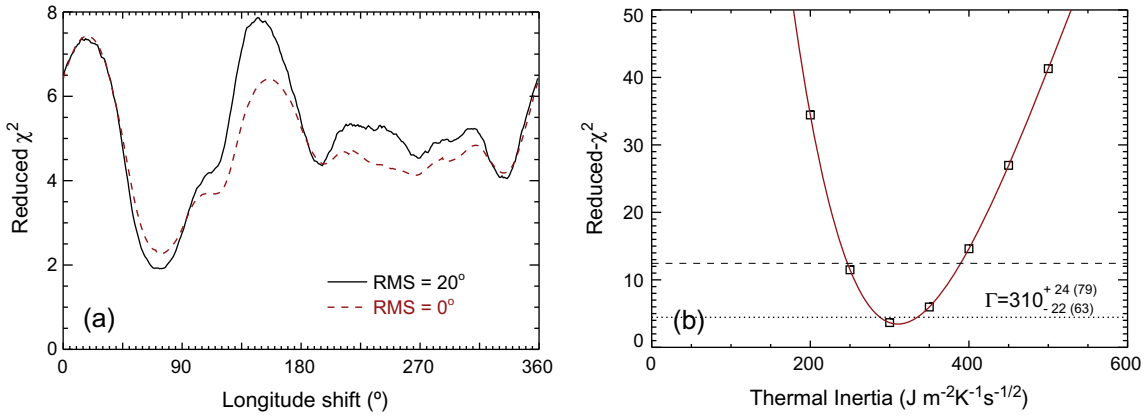

Fig. 10. (a) χ^2 goodness-of-fit as a function of longitude shift for the thermal models that include the radar shape. The best fit to the data occurs at a shift of ~74° between the (arbitrarily chosen) zero longitude for the radar shape and the start time of the IRAC photometric observations. The χ^2 curves here are for Γ = 250 for the smooth surface and Γ = 300 for the rough surface. (b) An example fit to χ^2 vs thermal inertia used to estimate thermal inertia at each longitude. The dotted line marks $\chi^2_{min}+1$ (1σ) and the dashed line marks $\chi^2_{min}+9$ (3σ). The 3σ uncertainties are given in parentheses.

Table 7
Results from TPM fits using radar shape.

Observation	Rot. phase[a]	RMS = 20°	
		Γ (J m^{-2} s$^{-1/2}$ K^{-1})	$\Delta\Gamma$[b] (J m^{-2} s$^{-1/2}$ K^{-1})
IRS #1	0.30–0.57		
IRS #2	0.79–0.06		
IRAC+PUI 1	0.0000	300	+19 −18
IRAC+PUI 2	0.0864	330	+24 −23
IRAC+PUI 3	0.1937	298	+15 −13
IRAC+PUI 4	0.2905	296	+18 −16
IRAC+PUI 5	0.3973	272	+19 −17
IRAC+PUI 6	0.4761	310	+24 −22
IRAC+PUI 7	0.6020	334	+25 −23
IRAC+PUI 8	0.6901	336	+23 −21
IRAC+PUI 9	0.7994	345	+19 −18
IRAC+PUI 10	0.8992	292	+24 −23
IRAC+PUI 11	0.9892	290	+19 −18
Average		*310*	*25*

Uncertainties of averages include standard deviation of values and propagation of uncertainties.

[a] Rotational phase relative to 1st IRAC AOR, calculated from the start time of each AOR. Repeated from Table 5 for ease of reference.

[b] Primary $\Delta\Gamma$ is region where $\chi^2 < \chi^2_{\min} + 1$.

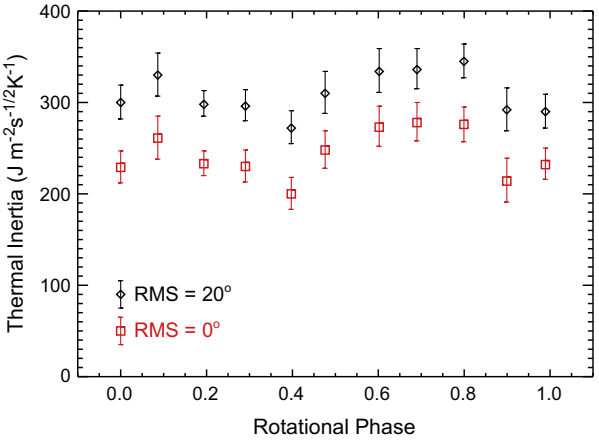

Fig. 11. Thermal inertia as a function of rotation, as derived using the radar shape and including surface roughness. The level of variation is comparable to the spherical case, but the rotational profile is different, now suggesting regions of low thermal inertia near rotational phases 0.4 and 0.9.

interpret, primarily because the cores of the silicate features are so strongly absorbing that the scattering regime transitions between volume and surface scattering as a very sensitive function of wavelength, grain size, and packing. As a result, spectral terminology often differs depending on the regime. Sample scientists and remote sensors observing bedrock or surfaces dominated by large grains (> a few hundred μm) refer to the Christiansen feature, restrahlen bands, and transparency features, which are related to transitions between volume and surface scattering as well as the specific vibrational modes. Observers of fine-grained, optically thin media (e.g., comet comae), on the other hand, are able to directly observe the Si–O vibrational bands in single-grain emission, which they generally refer to as resonance peaks. Regardless of the scattering regime, significant discoveries have been made from analysis of emissivity spectra of Mars (e.g., Christensen et al., 2001; Osterloo et al., 2008), asteroids (e.g., Emery et al., 2006; Lim et al., 2011; Vernazza et al., 2013), and comets (e.g., Hanner et al., 1994; Crovisier et al., 1997; Harker et al., 2007). We, likewise, search the IRS spectra of Bennu for spectral features diagnostic of surface mineralogy.

Emissivity spectra are computed by dividing the thermal flux spectra measured with IRS by the modeled thermal continua (Fig. 13). The *S*/*N* of the IRS spectra is highest in the SL1 module (7.5–14.1 μm); the observations were designed to be most sensitive in this wavelength range in order to search for silicate emissivity features. The LL2 data (14.1–20 μm) also have reasonably high *S*/*N*. Spectra from the shorter wavelength SL2 module and longer wavelength LL1 module are too noisy for useful mineralogical analysis, and are not considered here. A number of different thermal model continua for the IRS spectra are presented in the previous sections. They are all specifically fit to the IRS spectra and, particularly over the 7.5–20 μm wavelength range, vary only slightly in shape from one another. Emissivity spectra computed from the different continua all look very similar to one another, with minor differences in overall spectral slope, but no distinct spectral features.

The emissivity spectra of Bennu (Fig. 13) are featureless within the level of noise in the data. Upon close examination, a slight dip in the spectrum from observation #1 may be present near 13.5 μm, and a slight rise in the spectrum from observation #2 may occur at the same wavelength. These occur in the region of SL1 affected by an instrumental artifact, called the "teardrop",[6] so we do not consider them to be real mineralogical features.

We compare the emissivity spectra of Bennu with three other asteroids observed with Spitzer/IRS (Fig. 13). The S-type NEA Eros exhibits a weak (2–3%) emissivity plateau between about 8.4 and 10.5 μm (Vernazza et al., 2010). This feature is weak enough that a feature of similar strength could be masked by the noise in the spectra of Bennu. The downturn shortward of about 8.4 μm in the Eros spectrum, however, would be detected. The P-type Trojan asteroid Patroclus also exhibits a broad emissivity high, between about 9.3 and 11.9 μm (Mueller et al., 2010). Though still relatively weak, this feature would be detectable in the spectrum of Bennu. The D-type Trojan asteroid Hektor displays a very strong emissivity peak between about 9.3 and 11.9 μm (Emery et al., 2006) that would easily be detected in the Bennu data if present.

There are several potential interpretations for the absence of silicate features in these spectra. The first is that the surface of Bennu is devoid of silicates. Given that the mineralogy of all of the meteorite analogs for Bennu (Clark et al., 2011) is dominated by silicates of one type or another, we find this a very unlikely option. A second possibility is that silicate features are masked by low-albedo, opaque, featureless materials (e.g., carbonaceous material, magnetite). In the scattering regimes described above, spectral mixing in the MIR is generally linear, and silicates are already highly absorbing. Even though small amounts of opaque materials can diminish or completely mask spectral features in the visible and near infrared, a substantially larger abundance of opaques would be required to mask the silicate features in in the MIR. Furthermore, MIR spectra of analog meteorites clearly show spectral features that could rise

[6] http://irsa.ipac.caltech.edu/data/SPITZER/docs/irs/features/#8_SL1_14u_Teardrop.

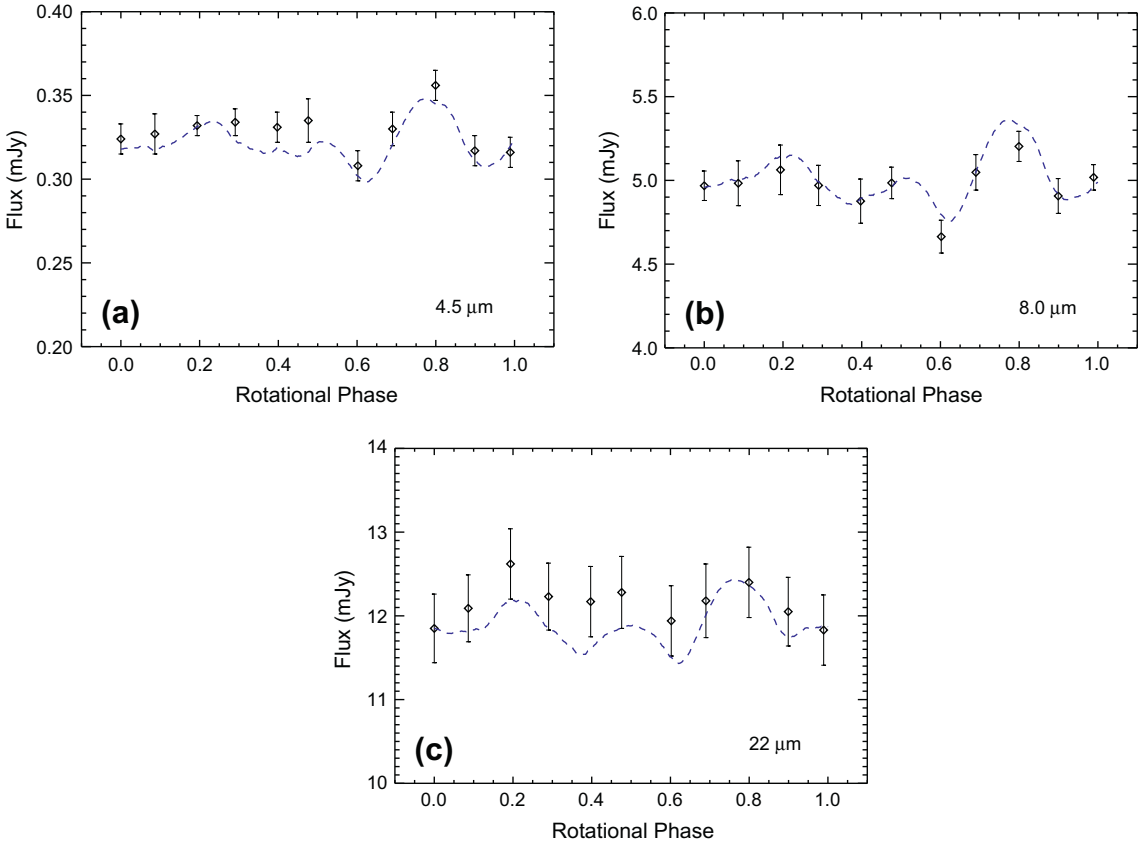

Fig. 12. Thermal lightcurves calculated with the TPM using the radar shape overplotted on IRAC data at (a) 4.5, (b) 8.0, and (c) 22 μm. The lightcurves are interpolated using the thermal inertias in Table 8 for reference.

above the noise in the IRS data (e.g., Salisbury et al., 1991), suggesting that this option is also not viable.

A third interpretation, and the one that we favor, is that a combination of surface grain size and packing state conspires to keep the spectral contrast of the silicate features very small. Laboratory experiments (e.g., Hunt and Logan, 1972) and Mie theory calculations (e.g., Harker et al., 2002) both reveal that single-grain emission cross sections for silicate materials in the MIR decrease in spectral contrast as particle size is increased from about a micron up to several tens of microns. When the grains are part of a regolith, the polarity of the emission feature near the Si–O fundamentals switches for large grains, such that for samples with average particle size greater than a few hundred microns, there is a clear emissivity low (with superposed reststrahlen features) reminiscent of the spectrum of a polished face or bedrock sample. Thick layers of small grains can also somewhat mimic this effect, decreasing the spectral contrast as compared to single-grain emissivity (Hunt and Logan, 1972). In fact, the only way to produce a spectrum like that of Hektor shown in Fig. 13 is for the surface to be composed of fine-grained (∼ μm-sized) particles that are well-separated from one another (e.g., in an extremely high porosity fairy-castle structure, embedded in a medium that is transparent in the MIR, or dispersed in an optically thin cloud or coma above the surface; Emery et al., 2006). The absence of such features from the spectra of Bennu indicates that the surface is not covered in such a fine-grained, fairy-castle regolith of silicate particles (spectral observations sense the upper few tens of microns to few millimeters, depending on the mean free photon path at a given wavelength). The absence of features of opposite polarity indicates the surface is not covered in bedrock or boulders of silicate material. The emissivity spectra are therefore inconclusive in terms of surface mineralogy, but they do place these broad constraints on the structure of the surface layer.

3.3. Coma search

We use the infrared images of Bennu obtained with Spitzer to perform a sensitive search for the presence of dust around the asteroid. The majority of NEAs do not show any evidence of such extended emission, but there are some exceptions. Most prominent among the exceptions is 3200 Phaethon, which is in the same taxonomic class (B-type) as Bennu (de León et al., 2010). Phaethon is the parent of the Geminid meteor shower, so has clearly shed dust at some point in its recent past. Furthermore, Jewitt and Li (2010) detected a brightening of Phaethon when it was 0.14 AU from the Sun, which they interpret as an impulsive release of dust. Jewitt et al. (2013) further report a dust tail imaged near perihelion passage of Phaethon in 2009 and 2012. In addition, a dusty coma around the asteroid would represent a potential hazard to safe operation of the spacecraft. Therefore, even though no dust is anticipated around Bennu, a search for a dust coma is conducted.

The peak-up images at 16 and 22 μm provide the most sensitive search for dust, because they sense the peak of the blackbody curve for dust at ∼1 AU. Radial profiles of all PUI frames are generated, using 0.2-pixel cubic spline interpolation, and co-added by wavelength to generate a super profile. The super profile is compared to a model point spread function (PSF) generated with the STinyTim[7] software for a 290 K blackbody spectrum. The 16 μm PSF was smoothed by the equivalent of a 1.9 pixel boxcar (1.5 pixels for

[7] http://irsa.ipac.caltech.edu/data/SPITZER/docs/dataanalysistools/tools/contributed/general/stinytim/.

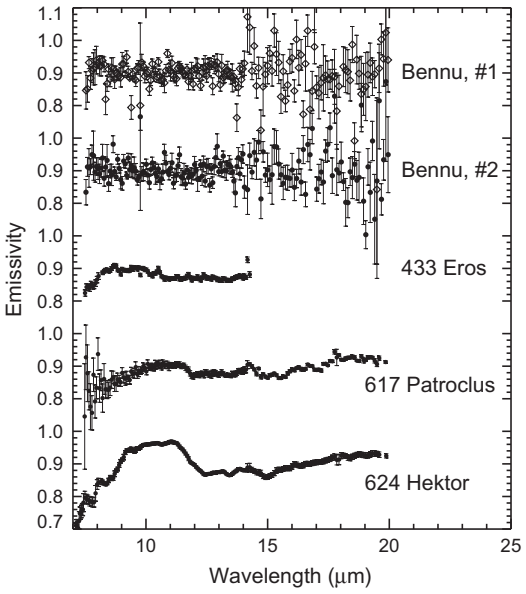

Fig. 13. Emissivity spectra of Bennu compared with those published for a few other asteroids. Only the SL1 (7.5–14.1 μm) and LL2 (14.1–20 μm) portions of the Bennu spectra are shown; the SL2 (5.2–7.5 μm) and LL1 (20–38 μm) portions have much lower *S*/*N*. The emissivity spectra of Bennu are featureless within the noise of the data. Features at the scale of those seen for Eros (Vernazza et al., 2010) could be present, but hidden in the noise, except possibly for the downturn from ~8.5 to 7.5 μm in Eros. Features comparable to those seen in the spectrum of Patroclus (Mueller et al., 2010) or Hektor (Emery et al., 2006) would have been detected.

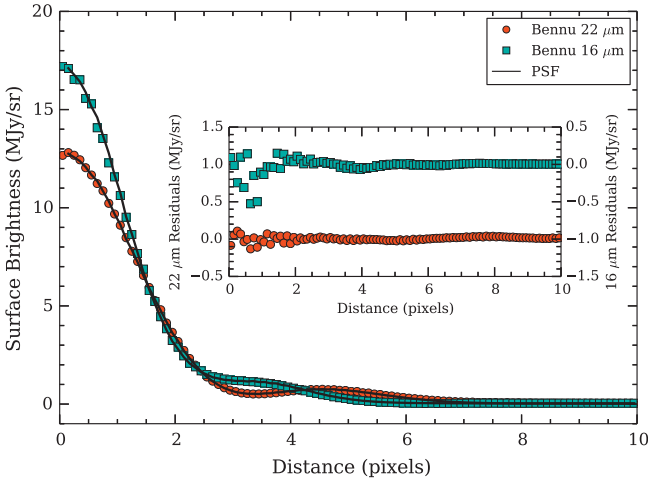

Fig. 14. Profiles from PUI 16 (blue squares) and 22 μm (red circles) images of Bennu compared to model PSF profiles. The inset shows the residuals from subtraction of the model PSF from the data profiles. No residual extended emission from dust is detected. (For interpretation of the references to color in this figure legend, the reader is referred to the web version of this article.)

22 μm), similar to the 1.8-pixel smoothing required by Engelbracht et al. (2007) for Spitzer's MIPS 24 μm camera. The model PSFs are fit to Bennu's super profiles, including a constant background term, for the range 1–5 pixels with the Blue channel, and 1–7 pixels for Red (Fig. 14). The scaled PSFs closely reproduce the profiles, except near the core where artifacts from the interpolation method are more apparent.

We conclude that the profiles indicate no detectable coma. The residual flux in the Blue channel within 7 pixels is -0.12 ± 0.15 MJy sr^{-1} and in the Red channel it is -0.01 ± 0.15 MJy sr^{-1}. Within an annulus of 7–10 pixels, the residuals for Blue and Red are -0.0032 ± 0.0078 MJy sr^{-1} pix^{-1} and -0.023 ± 0.009 MJy sr^{-1} pix^{-1}, respectively.

The upper limit to the coma flux is calculated using two different methods. First (method 1), we sum the residuals inside a 7-pixel radius. However, this method is subject to high frequency noise at the smallest distances. As an alternative (method 2), we scale a ρ^{-1} (1/distance) surface brightness profile to the measured residual brightness at 7–10 pixels from the asteroid, and sum the flux from this profile inside of 7 pixels (~4750 km). For both cases, the 3σ uncertainty is added to the summed flux to establish a 3σ upper limit. The upper-limit coma fluxes from method 1 are 0.58 and 0.47 mJy at 16 and 22 μm, respectively, and from method 2 0.48 and 0.72 mJy.

The limits on the coma flux are used to estimate upper limits on dust mass. With Mie theory, we compute temperatures and emission cross sections to estimate the flux from single grains or distributions thereof, and compare the grain fluxes to the upper-limit fluxes to limit the number of grains and total mass (e.g., Harker et al., 2002). Taking the larger of the two upper-limit fluxes from methods 1 and 2 (0.58 mJy and 0.72 mJy), we calculate the dust upper limits for six particle radii ranging from 0.01 to 1000 μm (assuming solid spheres). In addition, we also consider a power-law grain size distribution, $dn/da = a^{-3.5}$ (where a is grain radius), similar to those found in comet comae (Fulle, 2004; Economou et al., 2013). In Table 8, we present our results for two representative compositions: (1) amorphous (or disordered) carbon, representing any low albedo dust component; and (2) amorphous silicate of olivine composition, representing possible silicate dust species. Our optical constants for amorphous carbon are from Edoh (1983), and for amorphous olivine we use the sample with Fe/Mg ratio of 50/50 from Dorschner et al. (1995). No cometary activity from Bennu has been detected, therefore any putative gas-driven mass loss must be small. Therefore, we consider the mass limits assuming particles larger than a few tens of micrometers to be unreasonable, because of the difficulty to lift such large grains without a significant (comet-like) gas flux. Overall, we place an upper limit of order of magnitude 10^6 g within 4750 km on Bennu's dust coma.

4. Discussion

4.1. Thermophysical properties

The best estimate of the disk-integrated thermal inertia of Bennu is the average of the results from the model that includes radar shape and moderate surface roughness (Table 7). The uncertainties listed in Table 7 are the 1σ statistical uncertainties from χ^2 minimization. Three additional important sources of uncertainty must also be considered. The first is due to surface roughness. We take the thermal inertia values for the RMS = 0° and 66° to represent the 3σ range. Secondly, there is a fairly significant difference in the thermal inertias derived from the spectral and photometric data. The absolute flux calibration of the spectrograph is not as good as the cameras, and small pointing offsets can also lead to variations in spectral slope and relative scaling among the four orders that comprise the final spectrum. To be conservative in the uncertainty estimate, we also take the difference between the photometric and spectra results to represent a 3σ range. Thirdly, Nolan et al. (2013) point out that the polar axis of Bennu is the least-well constrained of the three axes of the shape model. This is due to symmetries in the radar return for equatorial viewing geometries, as was the case for both the 1999 and 2005 radar observations of Bennu. The polar diameter (508 ± 32 m) could be as large as the shortest equatorial diameter (535 ± 10 m); in other words, the oblateness could be close to zero. As a conservative estimate of the uncertainty from oblateness, we therefore consider the results for the spherical TPM to represent a 3σ range. Note that this is separate from the

Table 8
Upper limits on dust coma abundance and mass.

Radius (μm)	Blue (16 μm)			Red (22 μm)		
	F(a)[a] (mJy)	N(a)	Mass (g)	F(a)[a] (mJy)	N(a)	Mass (g)
Amorphous carbon grains						
0.01	5.55×10^{-23}	1.73×10^{22}	2.42×10^{5}	2.35×10^{-23}	7.84×10^{22}	8.21×10^{5}
0.10	5.90×10^{-20}	1.69×10^{19}	1.70×10^{5}	2.46×10^{-20}	7.47×10^{19}	7.82×10^{5}
1.00	2.57×10^{-17}	3.73×10^{16}	3.91×10^{5}	1.17×10^{-17}	1.57×10^{17}	1.65×10^{6}
10.00	3.83×10^{-15}	2.51×10^{14}	2.63×10^{6}	4.28×10^{-15}	4.30×10^{14}	4.50×10^{6}
100.00	3.48×10^{-13}	2.76×10^{12}	2.89×10^{7}	3.42×10^{-13}	5.38×10^{12}	5.63×10^{7}
1000.00	3.37×10^{-11}	2.85×10^{10}	2.98×10^{8}	3.16×10^{-11}	5.82×10^{10}	6.09×10^{8}
0.1–1000[b]	4.18×10^{-20}	2.30×10^{19}	4.77×10^{6}	2.98×10^{-20}	6.18×10^{19}	1.28×10^{7}
Amorphous silicate grains of olivine stoichiometry[c]						
0.01	7.56×10^{-23}	1.27×10^{22}	1.75×10^{5}	4.33×10^{-23}	4.25×10^{22}	5.88×10^{5}
0.10	1.20×10^{-19}	8.01×10^{18}	1.11×10^{5}	6.26×10^{-20}	2.94×10^{19}	4.06×10^{5}
1.00	5.09×10^{-17}	1.89×10^{16}	2.61×10^{5}	3.43×10^{-17}	5.36×10^{16}	7.41×10^{5}
10.00	4.32×10^{-15}	2.22×10^{14}	3.07×10^{6}	5.12×10^{-15}	3.59×10^{14}	4.97×10^{6}
100.00	4.22×10^{-13}	2.28×10^{12}	3.15×10^{7}	3.94×10^{-13}	4.67×10^{12}	6.45×10^{7}
1000.00	4.21×10^{-11}	2.28×10^{10}	3.15×10^{8}	3.62×10^{-11}	5.08×10^{10}	7.03×10^{8}
0.1–1000[b]	6.89×10^{-20}	1.39×10^{19}	3.82×10^{6}	5.28×10^{-20}	3.48×10^{19}	9.53×10^{6}

[a] Flux from a single grain of the given size.
[b] For a grain size distribution of $dn/da = a^{-3.5}$.
[c] Fe/Mg ratio of 50/50.

uncertainty contribution of $\pm 20\ J\ m^{-2}\ s^{-1/2}\ K^{-1}$ from radar size uncertainties described in Section 3.1.3. Folding all these uncertainties together, we estimate a bulk thermal inertia of Bennu of 310 ± 70 ($\pm 180\ 3\sigma$) $J\ m^{-2}\ s^{-1/2}\ K^{-1}$.

This result is somewhat lower than previous determinations of Bennu's thermal inertia. Emery et al. (2010) and Müller et al. (2012) report a somewhat higher thermal inertia for Bennu of $\sim 600\ J\ m^{-2}\ s^{-1/2}\ K^{-1}$. Both of those previous works used the Spitzer IRS data presented here, though with different relative scaling of the orders, but not the photometric data. (Müller et al. use the PUI data as presented in Emery et al. (2010) to infer ellipsoidal axial ratios, but do not include those fluxes in their thermal inertia solution. Note that the PUI calibration has been updated, and the older flux values are superseded by those presented in Section 2.3). Neither included the radar shape model, but rather assumed a spherical shape. Both studies considered the effects of roughness: Emery et al. (2010) used the same roughness implementation as used here, and Müller et al. (2012) used a parameterization also based on spherical-section craters. Müller et al. (2012) also included a ground-based photometric detection at 8.59 μm from the VLT and Herschel observations at 70, 100, and 160 μm. The long-wavelength Herschel data are not very sensitive to temperature, and the VLT observing conditions are described as sub-optimal.

One significant difference between those previous works and the current results is the inclusion of the real shape of Bennu rather than assuming a sphere. As described in Section 3.1.2 and discussed further below, the oblate shape of Bennu leads to a lower thermal inertia determination. A second difference is the use of the IRS data. As described in Section 2.2, low resolution IRS data can be difficult to properly scale. In the present analyses, we use a different set of scale factors than Emery et al. (2010). We have also chosen not to include the SL2 module in the thermal fits, because the S/N is very low. Müller et al. (2012) included the SL2 data in their analysis. Finally, the IRAC+PUI photometric data have much higher S/N, and we consider the results from thermal fits to the photometric data more reliable than those to the spectral data. The combination of these considerations in thermal modeling lead to the lower thermal inertia reported herein.

It is instructive to step through the results for important parameters to gain insight into the limitations of each technique and the overall uncertainties in the final results. Section 3.1 describes several thermal model techniques and a variety of parameters. Each technique is limited by assumptions inherent in the model as well as uncertainties in input parameters.

Using the NEATM analysis one finds a radius that is significantly larger than that measured by radar. The primary limitation of NEATM that leads to this erroneous result is the assumption of no night side emission. In addition, the assumption of spherical shape and parameterization of physical effects (surface roughness and heat conduction) by a simple beaming parameter also have an effect. The absence of emission from the night side leaves a flux deficit when a substantial portion of the night side is viewed. The model compensates by requiring an increased size to match the measured flux (Wolters and Green, 2009). Since p_v is calculated directly from the derived size, it must, likewise, be underestimated by NEATM at large phase angles. One must be careful with NEATM analysis of observations at large phase angles and of non-spherical bodies.

Including the effects of thermal inertia (i.e., explicitly modeling night side emission) and surface roughness, even while maintaining the assumption of spherical shape, provides a size estimate that is much closer to the radar-derived value. In fact, the variation in cross-sectional area with rotation from the model is in excellent agreement with the radar shape. Nevertheless, D_{eff} from the spherical TPM (484 m; Section 3.1.2) is about 2% smaller than the average radar D_{eff} for the viewing geometry of the Spitzer observations (496 m). The difference here is likely due to the oblateness of Bennu. The thermal inertia estimate from the spherical model is higher than found using the radar shape, and the rotational signature is also somewhat different. As described in Section 3.1.3, the higher thermal inertia when using the spherical shape is probably compensation for the oblateness of the asteroid. The different rotational signature of thermal inertia is also likely due to shape effects. The temperature and flux distributions on the real shape model depend critically on the orientation of surface facets relative to the Sun and observer. The spherical model will compensate for the variations in flux due to facet orientation with adjustments to the thermal inertia. Caution is therefore advised when interpreting the results of thermal models that assume spherical shape. We have not performed a systematic analysis of different shapes, but this case study of Bennu illustrates that even relatively small deviations from sphericity can lead to significant (~30%) errors in bulk thermal inertia and its rotational signature.

The ability of the TPM that includes shape and surface roughness to reproduce the overall thermal fluxes, the SEDs, and the

thermal lightcurves measured in 2007 is an indication that the radar shape and size, derived from radar imaging and visible photometry taken in 1999 and 2005, is accurate. The inversion of lightcurve and radar data to determine the shape assumed homogeneous visible albedo on the surface of Bennu. Although the thermal analyses presented here provide no reason to suspect anything other than a homogeneous albedo, the observations are not well suited to detect albedo variations. Simultaneous visible and thermal lightcurve observations, or observations taken close enough in time that they could be precisely phased given the uncertainty in rotation period, would be best for detecting any such heterogeneity. The heterogeneity that is suggested, that of thermal inertia, is relatively low amplitude (~20%, or 60 J m^{-2} K^{-1} s$^{-1/2}$) and, if real and truly due to thermal inertia, could be explained by relatively minor variations in average grain size on the surface (see Section 4.2). Nolan et al. (2013) report one possible 10–20 m boulder, which is too small to have a noticeable effect in disk-integrated thermal observations. The boulder is at relatively high latitudes and would be most visible at a rotational phase of ~0.5 in Fig. 11. The thermal inertia is neither at a maximum nor minimum there, confirming that the single boulder is not responsible for the apparent variability in thermal inertia. From the analysis presented here, it is possible that some amount of the thermal inertia variation is due to changes in surface roughness. In either case, our interpretation is that the surface is largely homogeneous, with perhaps only minor variations in grain size or surface roughness.

Thermal inertia estimates are now available for a growing number of asteroids over a broad size range. In general, large Main Belt asteroids ($D \gtrsim 100$ km) tend to have very low thermal inertias (~10 to 50 J m^{-2} K^{-1} s$^{-1/2}$; e.g., Spencer et al., 1989; Keihm et al., 2013), which is taken to indicate the presence of a well-developed, lunar-like regolith. Smaller NEAs, on the other hand, have thermal inertias that range from ~150 to nearly 1000, trending to higher values for smaller objects. For example, Eros has $\Gamma = 150 \pm 50$ (Mueller, 2007), 1999 JU$_3$, the target of the Hayabusa-2 mission, has Γ between 200 and 700 (Campins et al., 2009; Müller et al., 2011), and Itokawa has $\Gamma = 700 \pm 100$ (Mueller, 2007; Müller et al., 2005). Note that non-spherical shapes were included in the thermal models for these three well-studied NEAs. Main Belt asteroids in the size range 30–100 km appear to occupy a transition region in thermal inertia between very low and moderate (~100–200), perhaps indicating a transition between primordial bodies and those that have been substantially shattered (Delbó and Tanga, 2009). For regoliths on airless bodies where radiation is the dominant heat transport mechanism between grains, the thermal inertia is a function of temperature and therefore heliocentric distance (Γ is proportional to $r^{-3/4}$). An asteroid in the Main Belt whose surface is otherwise identical to an NEA at ~1 AU would thereby have a thermal inertia ~2 to 2.5 times lower than the NEA. The trend of higher thermal inertia with smaller sizes still holds taking this factor into account. Bennu's thermal inertia of 310 J m^{-2} K^{-1} s$^{-1/2}$ places it in the low end for NEAs. It is particularly low among those NEAs with $D \lesssim 2$ km, though it is important to note that the sample of small NEAs for which thermal inertia has been determined is limited. It will be very interesting to see the distribution of thermal inertias among small NEAs as more of them become better characterized.

4.2. Average grain size of the surface

Thermal inertia is a reasonably good indicator of the average grain size in the near-surface. This is particularly true for small, airless bodies such as asteroids, for which induration (as has occurred, for instance, through fluvial processes on Earth and Mars) of grains is less likely. The definition of "near-surface" here depends on the e-folding depth of the thermal wave penetrating the surface. For diurnal thermal waves on asteroids with rotation periods of a few to several hours, this depth is generally a few mm to a few tens of cm. The thermophysical properties of lunar regolith have been well-characterized. The average grain size in the lunar regolith is ~60 μm (Carrier et al., 1991), and the bulk thermal inertia is ~50 J m^{-2} K^{-1} s$^{-1/2}$ (Wesselink, 1948; Cremers, 1975; Langseth and Keihm, 1977). That large asteroids have similarly low thermal inertias leads to the inference that their regoliths are composed of similarly small grains. Typical silicate bedrock, on the other hand, has a thermal inertia around 2500 J m^{-2} K^{-1} s$^{-1/2}$ (Jakosky, 1986).

The thermal inertia of Bennu falls between the two "extreme" values of the lunar regolith on the low end and bedrock on the high end. Since the thermal inertia is less than bedrock, we can infer that the average grain size on Bennu is less than the thermal skin depth (the e-folding depth of the diurnal thermal wave). The thermal skin depth is given by

$$l_s \sim \frac{\Gamma}{c_p \rho}\sqrt{\frac{2}{\omega}}, \tag{4}$$

where Γ is thermal inertia, c_p is heat capacity, ρ is grain density, and ω is rotation rate. For the 1σ range of thermal inertias for Bennu, and for reasonable estimates of c_p (500 J kg^{-1}K^{-1}; Opeil et al., 2010, 2012) and ρ (2500 kg m^{-3}; Macke et al., 2011), we estimate the thermal skin depth on Bennu to be ~1.3 to 2.1 cm. From radar polarization and albedo measurements, Nolan et al. (2013) estimate a grain density of 1800 kg m^{-3} for Bennu's surface. Considering ranges of ρ from 1500 to 3500 kg m^{-3} increases the range of l_s to ~1.0 to 3.6 cm. The inference, then, is that the average grain size is less than 3.6 cm, and likely less than 1 cm. Since the thermal inertia is also significantly higher than the lunar value, we infer that the average grain size is larger than that of the lunar regolith. Qualitatively, it appears likely that the average grain size at the surface of Bennu is somewhere in the range of a few tenths of a mm to several mm.

A question that arises is whether the bedrock thermal inertia value of 2500 J m^{-2} K^{-1} s$^{-1/2}$ holds for Bennu, for which the closest meteoritic analog is thought to be CM or CI carbonaceous chondrites (Clark et al., 2011). Opeil et al. (2010) report thermal conductivity measurements of a small (3 × 6 × 2 mm) section of the CM meteorite Cold Bokkeveld. They find a very low thermal conductivity of 0.5 W m^{-1} K^{-1}, which, assuming c_p of 500 J kg^{-1} K^{-1} and ρ of 2360 kg m^{-3} (Opeil et al., 2012), corresponds to Γ = 768 J m^{-2} K^{-1} s$^{-1/2}$ as a bedrock value. The only other carbonaceous meteorite for which they measured a thermal conductivity is NWA 5515, a CK chondrite, not considered to be an analog for Bennu. Nevertheless, the thermal conductivity of NWA 5515 is 1.48 W m^{-1} K^{-1}, corresponding to bedrock Γ of ~1450 J m^{-2} K^{-1} s$^{-1/2}$. These are much lower than the canonical 2500, but in either case, the measured Γ for Bennu is still significantly lower than the bedrock value. Though the quantitative estimate of grain size might change, the qualitative assessment that the average grain size must be smaller than ~1.0 to 3.6 cm still holds.

An interesting comparison point is asteroid (25143) Itokawa. Though differently shaped and a different spectral (compositional) type than Bennu, the two asteroids have similar sizes. Images of Itokawa returned by the Hayabusa spacecraft reveal that many regions of the surface contain abundant boulders, and the finest-grained "seas" appear to be dominated by grains that are a few cm in diameter, though the spacecraft did return samples that were a few hundred microns and smaller (Miyamoto et al., 2006; Tsuchiyama et al. 2011). With a rotation period of 12.1323 h (Ďurech et al., 2008), Γ of 700 J m^{-2} K^{-1} s$^{-1/2}$ (Mueller, 2007; Müller et al., 2005), and assuming c_p of 500 J kg^{-1} K^{-1} and ρ of 3500 kg m^{-3} (Opeil et al., 2012), l_s for Itokawa is ~4.7 cm. Similar logic as applied to Bennu would indicate an average grain size of

around a couple of cm for Itokawa, which is consistent with imaging so long as the thermal observations were dominated by flux from the seas (or if unresolved cm-sized pebbles or dust coatings are prevalent among apparently boulder-rich regions that were not imaged at the highest spatial resolution).

Gundlach and Blum (2012, 2013) developed an analytical methodology for quantitatively estimating an average regolith grain size from thermal inertia measurements. The basic formulation considers heat transferred by conduction across grain boundaries and by radiation through the voids between grains. Grain contact areas (which affect the grain-to-grain thermal conductivity) are adjusted for deformation due to forces between grains according to Hertz theory, with corrections for non-gravitational forces and non-spherical shapes included parametrically. The solution method consists of: (1) computing the effective regolith thermal conductivity from the measured Γ from $\Gamma = \sqrt{kc_p\rho\phi}$, where k is the thermal conductivity, ρ and c_p are density and heat capacity, respectively, and ϕ is a packing fraction (1-porosity); (2) calculating a modeled thermal conductivity as a function of grain size, as presented in Eq. (5) of Gundlach and Blum (2013); (3) comparing the measured and modeled thermal conductivities to find the grain size where they agree. Since the packing fraction of the regolith is unknown, calculations are made for a range of ϕ from 0.1 to 0.6. We mimic their calculation scheme, including values for many parameters as given in Gundlach and Blum (2013), but inserting the thermal inertia and surface temperature for Bennu derived herein. Fig. 15 illustrates the results of the calculations, which suggest an average grain radius of about 0.35 cm (0.28–0.63 cm). There are many uncertainties and assumptions in the development of the analytical expression and the parameters used. The formal uncertainties are difficult to estimate, but may be, as a rule of thumb, +100%/−50% (J. Blum, personal communication). For the 1σ range in Γ and the full range of ϕ, the grain size estimated in this way ranges from 0.17 to 0.95 cm.

From both a qualitative and quantitative approach, we conclude that the measured thermal inertia of Bennu indicates abundant sub-cm sized particles on the surface. The estimates here assume a mono-disperse regolith. In reality, the regolith is probably comprised of grains with some size distribution. The radar observations rule out boulders larger than ~7.5 m, but do not constrain the abundance of smaller boulders. The presence of meter-scale boulders on the surface would not change the conclusion that sub-cm sized particles must also be abundant. This average grain size is consistent with the interpretation that the absence of silicate features in the emissivity spectrum is due to grain size and regolith packing state; the intermediate grain sizes between fine dust and bedrock (or cobble-scale boulders) are the right approximate scale for causing a low spectral contrast, hiding features below the level of noise in the IRS spectra. However, it is important to note that the spectral observations sense only the uppermost tens of microns to few millimeters of the surface, whereas the thermal inertia estimate averages over a depth of a couple of centimeters (the thermal skin depth). Nolan et al. (2013) note that the radar polarization ratios of Bennu at radar wavelengths of 3.5 and 12.6 cm are lower than most other asteroids, including Itokawa, Eros, and 2005 YU_{55}. They conclude from this, and from the observation that the polarization ratios of Bennu at the two wavelengths are similar to one another, that the surface of Bennu is dominated by grains smaller than 3.5 cm, in agreement with our estimates from thermal inertia.

Recall that the thermophysical modeling in Section 3.1.3 suggests a possible heterogeneity in thermal inertia of about ±60 J m^{-2} K^{-1} s$^{-1/2}$. If this is a real signature of thermal inertia variability, and if that variability is due to grain size, according to the Gundlach and Blum (2013) methodology, a variation of only 0.05 cm in average grain size would be required. For all practical purposes, the surface of Bennu appears, at least from the observations presented here, to be quite longitudinally homogeneous.

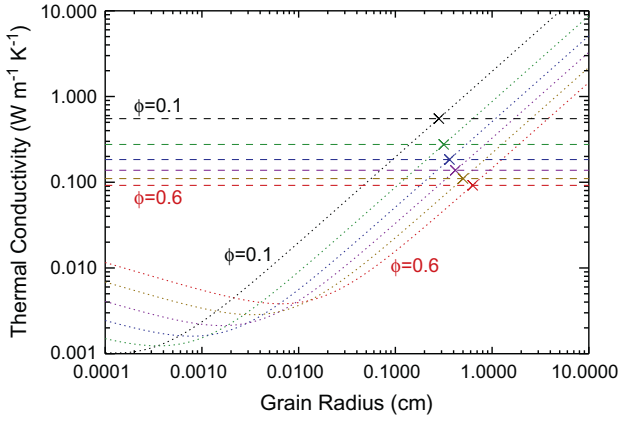

Fig. 15. Illustration of grain size estimates for Bennu according to the methodology of Gundlach and Blum (2013). Dashed lines indicate the regolith thermal conductivity computed from the measured thermal inertia (310 J m^{-2} K^{-1} s$^{-1/2}$). Dotted lines are model thermal conductivities as a function of grain size, from the Gundlach and Blum (2013) model. Xs mark the where the model thermal inertias match the "measured" values for a given packing fraction (ϕ); reading down to the *x*-axis from the Xs gives the grain size. Computations are made for ϕ ranging from 0.1 to 0.6 in intervals of 0.1.

5. Application to OSIRIS-REx

The results of this investigation are critical to OSIRIS-REx mission success. The direct measurement of thermal flux and the derived thermal inertia values provide explicit input into the mission asteroid thermal model. This product is included in the mission Environmental Requirements Document and is used by the teams developing the science instruments and the spacecraft to verify instrument performance in a relevant environment. In addition, the constraint on grain size played a major role in the design of the sample acquisition mechanism, which is capable of ingesting particles several centimeters in diameter. Determination of the low values for the geometric and bond albedos confirms our spectral analyses suggesting that Bennu is related to primitive carbonaceous chondrites. Furthermore these parameters feed into the design of the camera systems and the science lidar instrument. Finally, the lack of dust detection indicates a low risk of spacecraft hazards in the vicinity of Bennu. The upper limit for dust detection informs the mission search strategy; we will make sure the operational area around Bennu is clear prior to beginning proximity operations.

6. Conclusions

The surface of (101955) Bennu will be revealed to humankind when the OSIRIS-REx spacecraft arrives in 2018 and begins its exhaustive characterization in preparation for sampling. The chemical and mineralogical nature of the surface grains will become even clearer when OSIRIS-REx returns samples of the regolith to Earth in 2023. Until that time, however, inferences of surface properties rely on telescopic observations of Bennu, mostly as a point-source, as presented in the present work. Analysis of the thermal observations strongly suggests that OSIRIS-REx will send back images of a surface unlike any that we have seen in previous missions.

The thermal inertia of 310 ± 70 J m^{-2} K^{-1} s$^{-1/2}$ is significantly higher than found for the regolith-covered Eros, and significantly

lower than the cobble- and boulder-rich surface of Itokawa. Qualitative and quantitative arguments indicate that the most likely average grain size is somewhere between a millimeter and a centimeter, consistent with inferences from radar polarization (Nolan et al., 2013). Bennu also has a low visible albedo; using the absolute magnitude found by Hergenrother et al. (2013) of $H_v = 20.51$ and the effective diameter from thermal modeling, the visible geometric albedo (p_v) is 0.046 ± 0.005, consistent with the interpretation of Clark et al. (2011) that Bennu is a carbonaceous asteroid. The rotational coverage of the thermal observations reveals no significant longitudinal heterogeneity. If the slight variation in thermal inertia with rotation is real, it indicates a maximum change in grain size of about a millimeter. Observations at different epochs could be useful for constraining latitudinal heterogeneity. Spectroscopy in the 7.5–20 μm range is inconclusive in terms of surface mineralogy. The absence of silicate spectral features could indicate the absence (or low abundance) of silicates, but our preferred interpretation is that the featureless spectra are due to a moderate grain size and non-fluffy surface texture, consistent with the inference from thermal inertia. Thermal imaging reveals no indication of a dust coma, consistent with Bennu's asteroidal nature, and we place an upper limit of about 10^6 g of dust within 4750 km of Bennu.

Systematic analyses using several common thermal modeling approaches illustrate common pitfalls to be aware of for each approach. These have been discussed previously by other authors, and the high quality of the data of Bennu from Spitzer highlights them once more. Sizes and albedos derived using the relatively simple NEATM from observations at high phase angles should be used cautiously; the assumption of no night emission skews the results to larger size and lower albedo as more of the night side is observed. If the spin state is known, a thermophysical model alleviates this problem by modeling and explicitly including thermal emission from the night side. However, if a spherical shape is assumed for a non-spherical body to constrain bulk thermal inertia, errors of several tens of percent are possible, even if the actual shape is somewhat close to a sphere, as is the case for Bennu. The modest oblateness leads to an overestimate of thermal inertia by ~30% if a spherical shape is assumed. Analyses of rotational variability in thermophysical properties using a spherical shape can lead to spurious signatures. The detailed temperature distribution at a given rotational phase depends critically on the orientation of surface facets. When high quality data permit detailed thermal modeling of an asteroid, it can be quite important to consider the actual shape, depending on the goals of the analysis.

There is little doubt that Bennu will surprise us as we explore this small asteroid in ever increasing detail over the next decade, and on into the future with continued investigations using archived sample. Indeed, the results and predictions presented here will be put to the test as images of the surface of Bennu are returned, and even more directly by the detailed thermophysical analysis that will be enabled by high spatial resolution observations with the OSIRIS-REx Thermal Emission Spectrometer (OTES). Along with detailed characterization of Bennu itself, those spacecraft results will provide ground-truth calibration to telescopic observations like those presented here, enhancing understanding of the wider asteroid population.

Acknowledgments

We are grateful to Marco Delbó and Ben Rozitis for helpful discussions of this work. This work is based [in part] on observations made with the Spitzer Space Telescope, which is operated by the Jet Propulsion Laboratory, California Institute of Technology under a contract with NASA. This research made use of Tiny Tim/Spitzer, developed by John Krist for the Spitzer Science Center. Support for this work was provided by NASA through an award issued by JPL/Caltech. This work was also supported by NASA Contracts NNM10AA11C (DS Lauretta PI) through the New Frontiers Program and NNM07AB49P (MJ Drake PI) through the NASA Discovery Program. JPE appreciates funding from the NASA Planetary Geology & Geophysics program, Grant No. NNX08BA78G.

References

Bevington, P.R., Robinson, D.K., 2003. Data Reduction and Error Analysis for the Physical Sciences, third ed. McGraw-Hill, New York, pp. 194–217.
Binzel, R.P., Rivkin, A.S., Stuart, J.S., Harris, A.W., Bus, S.J., Burbine, T.H., 2004a. Observed spectral properties of near-Earth objects: Results for population distribution, source regions, and space weathering processes. Icarus 170, 259–294.
Binzel, R.P. et al., 2004b. Dynamical and compositional assessment of near-Earth object mission targets. Meteorit. Planet. Sci. 39, 351–366.
Binzel, R.P. et al., 2010. Earth encounters as the origin of fresh surfaces on near-Earth asteroids. Nature 463, 331–334.
Bottke Jr., W.F., Morbidelli, A., Jedicke, R., Petit, J.-M., Levison, H.F., Michel, P., Metcalfe, T.S., 2002. Debiased orbital and absolute magnitude distribution of the near-Earth objects. Icarus 156, 399–433.
Brent, R.P., 1973. Algorithms for Minimization without Derivatives. Englewood Cliffs, Prentice-Hal, NJl (Chapter 5).
Bus, S.J., Binzel, R.P., 2002. Phase II of the small main-belt asteroid spectroscopic survey. Icarus 158, 146–177.
Campins, H. et al., 2009. Spitzer observations of spacecraft target 162173 (1999 JU3). Astron. Astrophys. 503, L17–L20.
Campins, H. et al., 2010a. Water ice and organics on the surface of the Asteroid 24 Themis. Nature 464, 1320–1321.
Campins, H., Morbidelli, A., Tsiganis, K., de León, J., Licandro, J., Lauretta, D., 2010b. The origin of Asteroid 101955 (1999 RQ36). Astrophys. J. 721 (1), L53–L57.
Carrier III, D.W., Olhoeft, G.R., Mendell, W., 1991. Physical properties of the lunar surface. In: Heiken, Vaniman, French (Eds.), The Lunar Sourcebook. Cambridge Univ. Press, Cambridge, UK, pp. 475–594.
Chesley et al., 2013. Orbit and bulk density of the OSIRIS-REx target Asteroid (101955) Bennu. Icarus (in press).
Christensen, P.R. et al., 2000. A thermal emission spectral library of rock forming minerals. J. Geophys. Res. 105 (E4), 9735–9739.
Christensen, P.R. et al., 2001. Mars Global Surveyor Thermal Emission Spectrometer experiment: Investigation description and surface science results. J. Geophys. Res. 106 (E10), 23823–23871.
Clark, B.E. et al., 2010. Spectroscopy of B-type asteroids: Subgroups and meteorite analogs. J. Geophys. Res. 115, E06005. http://dx.doi.org/10.1029/2009JE003478.
Clark, B.E. et al., 2011. Asteroid (101955) 1999 RQ36: Spectroscopy from 0.4 to 2.4 μm and meteorite analogs. Icarus 216, 462–475.
Cremers, C.J., 1975. Thermophysical properties of Apollo 14 fines. J. Geophys. Res. 80, 4466–4470.
Crovisier, J. et al., 1997. The spectrum of Comet Hale–Bopp (C/1995 O1) observed with the Infrared Space Observatory at 2.9 Astronomical Units from the Sun. Science 275, 1904–1907.
Davies, J.K., Harris, A.W., Rivkin, A.S., Wolters, S.D., Green, S.F., McBride, N., Mann, R.K., Kerr, T.H., 2007. Near-infrared spectra of 12 near-Earth objects. Icarus 186, 111–125.
de León, J., Campins, H., Tsiganis, K., Morbidelli, A., Licandro, J., 2010. Origin of the near-Earth asteroid Phaethon and the Geminids meteor shower. Astron. Astrophys. 513, A26, 7pp.
de León, J., Pinilla-Alonso, N., Campins, H., Licandro, J., Marzo, G.A., 2012. Near-infrared spectroscopic survey of B-type asteroids: Compositional analysis. Icarus 218, 196–206.
Delbó, M., Tanga, P., 2009. Thermal inertia of main belt asteroids smaller than 100 km from IRAS data. Planet. Space Sci. 57, 259–265.
Delbó, M., dell'Oro, A., Harris, A.W., Mottola, S., Mueller, M., 2007. Thermal inertia of near-Earth asteroids and implications for the magnitude of the Yarkovsky effect. Icarus 190, 236–249.
DeMeo, F.E., Carry, B., 2013. The taxonomic distribution of asteroids from multi-filter all-sky photometric surveys. Icarus 226, 723–741.
Dorschner, J., Begemann, B., Henning, Th., Jager, C., Mutschke, H., 1995. Steps toward interstellar silicate mineralogy. II. Study of Mg–Fe–silicate glasses of variable composition. Astron. Astrophys. 300, 503–520.
Ďurech, J. et al., 2008. New photometric observations of Asteroids (1862) Apollo and (25143) Itokawa – An analysis of YORP effect. Astron. Astrophys. 488, 345–350.
Economou, T.E., Green, S.F., Brownlee, D.E., Clark, B.C., 2013. Dust Flux Monitor Instrument measurements during Stardust-NExT flyby of Comet 9P/Tempel 1. Icarus 222, 526–539.
Edoh, O., 1983. Ph.D. Dissertation, Dept. of Physics, Univ. Arizona.
Emery, J.P., Sprague, A.L., Witteborn, F.C., Colwell, J.E., Kozlowski, R.W.H., Wooden, D.H., 1998. Mercury: Thermal modeling and mid-infrared (5–12 μm) observations. Icarus 136, 104–123.
Emery, J.P., Cruikshank, D.P., Van Cleve, J., 2006. Thermal emission spectroscopy (5.2–38 μm) of three Trojan asteroids with the Spitzer Space Telescope: Detection of fine-grained silicates. Icarus 182, 496–512.

Emery, J.P. et al., 2010. Thermophysical characterization of potential spacecraft target (101955) 1999 RQ36. Lunar Planet. Sci. 41. Abstract #1533.
Engelbracht, C.W. et al., 2007. Absolute calibration and characterization of the multiband imaging photometer for *Spitzer*. I. The stellar calibrator sample and the 24 μm calibration. Publ. Astron. Soc. Pac. 119, 994–1018.
Fazio et al., 2004. The Infrared Array Camera (IRAC) for the Spitzer Space Telescope, 2004. Astrophys. J. Suppl. Ser. 154, 10–17.
Frölich, C., 2009. Evidence of a long-term trend in total solar irradiance. Astron. Astrophys. 501, L27–L30.
Fulle, M., 2004. Motion of cometary dust. In: Festou, M.C., Keller, H.U., Weaver, H.A. (Eds.), Comets II. The University of Arizona Press, Tucson, pp. 565–575.
Gundlach, B., Blum, J., 2012. Outgassing of icy bodies in the Solar System – II: Heat transport in dry, porous surface dust layers. Icarus 219, 618–629.
Gundlach, B., Blum, J., 2013. A new method to determine the grain size of planetary regolith. Icarus 223, 479–492.
Hanner, M.S., Lynch, D.K., Russell, R.W., 1994. The 8–13 μm spectra of comets and the composition of silicate grains. Astrophys. J. 425, 274–285.
Harker, D.E., Wooden, D.H., Woodward, C.E., Lisse, C.M., 2002. Grain properties of Comet C/1995 O1 (Hale–Bopp). Astrophys. J. 580, 579–597.
Harker, D.E., Woodward, C.E., Wooden, D.H., 2007. The dust grains from 9P/Tempel 1 before and after the encounter with deep impact. Science 310, 278–280.
Harris, A.W., 1998. A thermal model for near-Earth asteroids. Icarus 131, 291–301.
Hergenrother, C.W. et al., 2013. Lightcurve, color and phase function photometry of the OSIRIS-REx target Asteroid (101955) Bennu. Icarus 226, 663–670.
Houck, J. et al., 2004. The infrared spectrograph on the Spitzer Space Telescope. Astrophys. J. Suppl. Ser. 154, 18–24.
Hunt, G.R., Logan, L.M., 1972. Variation of single particle mid-infrared emission spectrum with particle size. Appl. Opt. 11, 142–147.
Jakosky, B.M., 1986. On the thermal properties of martian fines. Icarus 66, 117–124.
Jewitt, D., Li, J., 2010. Activity in Geminid Parent (3200) Phaethon. Astron. J. 140, 1519–1527.
Jewitt, D., Li, J., Agarwal, J., 2013. The dust tail of Asteroid (3200) Phaethon. Astrophys. J. 771 (article id L36) 5pp.
Keihm, S., Kamp, L., Gulkis, S., Hofstadter, M., Lee, S., Janssen, M., Choukroun, M., 2013. Reconciling Main Belt asteroid spectral flux density measurements with a self-consistent thermophysical model. Icarus 226, 1086–1102.
Langseth, M.G., Keihm, S.J., 1977. Lunar heat-flow experiment. NASA technical report NASA-CR-151619, CU-4-77.
Larson, H.P., Feierberg, M.A., Lebofsky, L.A., 1983. The composition of Asteroid 2 Pallas and its relation to primitive meteorites. Icarus 56, 398–408.
Lebofsky, L.A., Spencer, J.R., 1989. Radiometry and thermal modeling of asteroids. In: Binzel, R.P., Gehrels, T., Matthews, M.S. (Eds.), Asteroids II. The University of Arizona Press, Tucson, pp. 128–147.
Lim, L.F., Emery, J.P., Moskovitz, N.A., 2011. Spitzer IRS (5–30 μm) spectra of basaltic Asteroid 956 Elisa: Mineralogy and thermal properties. Icarus 213, 510–523.
Macke, R.J., Consolmagno, G.J., Britt, D.T., 2011. Density, porosity, and magnetic susceptibility of carbonaceous chondrites. Meteorit. Planet. Sci. 46, 1842–1862.
Mainzer, A. et al., 2011a. NEOWISE observations of near-Earth objects: Preliminary results. Astrophys. J. 743 (article id 156) 17pp.
Mainzer, A. et al., 2011b. Preliminary results from NEOWISE: An enhancement to the wide-field infrared survey explorer for Solar System science. Astrophys. J. 731 (article id 53) 13pp.
Milani, A., Chesley, S.R., Sansaturio, M.E., Bernardi, F., Valsecchi, G.B., Arratia, O., 2009. Long term impact risk for (101955) 1999 RQ36. Icarus 203 (2), 460–471.
Miyamoto, H. et al., 2006. Regolith migration and sorting on asteroid Itokawa. Science 316, 1011–1014.
Morrison, D., 1973. Determination of radii of satellites and asteroids from radiometry and photometry. Icarus 19, 1–14.
Morrison, D., 1974. Radiometric diameters and albedos of 40 asteroids. Astrophys. J. 194, 203–212.
Mueller, M., 2007. Surface Properties of Asteroids from Mid-Infrared Observations and Thermophysical Modeling. PhD Dissertation, Freie Universitaet Berlin. <http://www.diss.fu-berlin.de/2007/471/indexe.html>.
Mueller, M., Marchis, R., Emery, J.P., Harris, A.W., Mottola, S., Hestroffer, D., Berthier, J., di Martino, M., 2010. Eclipsing binary Trojan asteroid Patroclus: Thermal inertia from Spitzer observations. Icarus 205, 505–515.
Müller, T.G., Sekiguchi, T., Kaasalainen, M., Abe, M., Hasegawa, S., 2005. Thermal infrared observations of the Hayabusa spacecraft target Asteroid 25143 Itokawa. Astron. Astrophys. 443, 347–355.
Müller, T.G. et al., 2011. Thermo-physical properties of 162173 (1999 JU3), a potential flyby and rendezvous target for interplanetary missions. Astron. Astrophys. 525, A145, 6pp.
Müller, T.G. et al., 2012. Physical properties of OSIRIS-REx target Asteroid (101955) 1999 RQ_{36} derived from Herschel, VLT/VISIR, and Spitzer observations. Astron. Astrophys. 548, A36, 9pp.
Nolan, M.C., Magri, C., Howell, E.S., Benner, L.A.M., Giorgini, J.D., Hergenrother, C.W., Hudson, R.S., Lauretta, D.S., Margo, J.-L., Ostro, S.J., Scheeres, D.J., 2013. Shape model and surface properties of the OSIRIS-REx target Asteroid (101955) Bennu from radar and lightcurve observations. Icarus 226, 629–640.
Opeil, C.P., Consolmagno, G.J., Britt, D.T., 2010. The thermal conductivity of meteorites: New measurements and analysis. Icarus 208, 449–454.
Opeil, C.P., Consolmagno, G.J., Safarik, D.J., Britt, D.T., 2012. Stony meteorite thermal properties and their relationship with meteorite chemical and physical states. Meteorit. Planet. Sci. 47, 319–329.
Osterloo, M.M. et al., 2008. Chloride-bearing materials in the southern highlands of Mars. Science 319, 1651–1654.
Press, W.H., Flannery, B.P., Teukolsky, S.A., Vetterling, W.T., 1992. Numerical Recipes in C: The Art of Scientific Computing. Cambridge Univ. Press., New York, pp. 397–405, 689–699.
Rivkin, A.S., Emery, J.P., 2010. Detection of ice and organics on an asteroidal surface. Nature 64, 1322–1323.
Salisbury, J.W., D'Aria, D.M., Jarosewich, E., 1991. Midinfrared (2.5–13.5 μm) reflectance spectra of powdered stony meteorites. Icarus 92, 280–297.
Salisbury, J.W., Walter, L.S., Vergo, N., D'Aria, D.M., 1992. Mid-infrared (2.1–25 μm) Spectra of Minerals. Johns Hopkins Univ. Press, Baltimore, MD, 346pp.
Spencer, J.R., 1990. A rough-surface thermophysical model for airless planets. Icarus 83, 27–38.
Spencer, J.R., Lebofsky, L.A., Sykes, M.V., 1989. Systematic biases in radiometric diameter determinations. Icarus 78, 337–354.
Stuart, J.S., Binzel, R.P., 2004. Bias-corrected population, size distribution, and impact hazard for the near-Earth objects. Icarus 170, 295–311.
Tedesco, E.F., Noah, P.V., Noah, M., Price, S.D., 2002. The supplemental IRAS minor planet survey. Astron. J. 123, 1056–1085.
Trilling, D.E. et al., 2010. ExploreNEOs I. Description and first results from the warm Spitzer near-Earth object survey. Astron. J. 140, 770–784.
Tsuchiyama, A. et al., 2011. Three-dimensional Structure of Hayabusa Samples: Origin and evolution of Itokawa regolith. Science 333, 1125–1128.
Vernazza, P., Carry, B., Emery, J., et al., 2010. Mid-infrared spectral variability for compositionally similar asteroids: Implications for asteroid particle size distributions. Icarus 207, 800–809.
Vernazza, P., Fulvio, D., Brunetto, R., Emery, J.P., Dukes, C.A., Cipriani, F., Witasse, O., Schaible, M., Zanda, B., Strazzulla, G., Baragiola, R.A., 2013. Paucity of Tagish Lake-like parent bodies in the Asteroid Belt and among Jupiter Trojans. Icarus 225, 517–525.
Walsh, K.J., Delbó, M., Bottke, W.F., Vokrouhlický, Lauretta, D.S., 2013. Introducing the Eulalia and new Polana asteroid families: Re-assessing primitive asteroid families in the inner Main Belt. Icarus 225, 283–297.
Werner, M.W. et al., 2004. The Spitzer space telescope mission. Astrophys. J. Suppl. Ser. 154, 1–9.
Wesselink, A.J., 1948. Heat conductivity and the nature of the lunar surface material. Bull. Astron. Soc. Neth. 10, 351–363.
Wolters, S.D., Green, S.F., 2009. Investigation of systematic bias in radiometric diameter determination of near-Earth asteroids: The night emission simulated thermal model (NESTM). Mon. Not. R. Astron. Soc. 400, 204–218.
Wolters, S.D., Green, S.F., McBride, N., Davies, J.K., 2008. Thermal infrared and optical observations of four near-Earth asteroids. Icarus 193, 535–552.
Ziffer, J., Campins, H., Licandro, J., Walker, M.E., Fernández, Y., Clark, B.E., Mothe-Diniz, T., Howell, E., Deshpande, R., 2011. Near-infrared spectroscopy of primitive asteroid families. Icarus 213, 538–546.